scientific reports

Check for updates

OPEN

Thermohydrodynamic analysis of magnetorheological conical bearings with conjugated heat transfer

Seyyed Amirreza Vaziri[1], Mahmood Norouzi[1], Pooria Akbarzadeh[1], Kyung Chun Kim[2] & Mirae Kim[2,3]✉

This study presents a comprehensive investigation into a 3D simulation of magnetorheological (MR) conical bearings, focusing on considering viscous dissipation using the conjugated heat transfer approach. The behavior of MR fluids is expressed through the utilization of the Bingham-Papanastasiou constitutive equation. Notably, this study considers variations in viscosity and yield stress as functions of both magnetic field intensity and temperature. The study utilizes a multidisciplinary approach, encompassing fluid dynamics, magnetism, and heat transfer, to model and analyze the behavior of MR fluids within conical bearing geometries. The governing equations containing Cauchy momentum, energy, and Maxwell equations are solved using the finite element method. This research delves into the impacts of viscous dissipation on the functional and characteristic attributes of conical bearings. The energy equations in solid and fluid domains and extended considerations to the plug region within viscous dissipation are specifically addressed. Extensive validation is performed through a comparative analysis involving experimental, numerical, and analytical studies to ensure the validity of results. The results reveal the substantial impact of temperature on both the characteristics and functionality of magnetorheological conical bearings.

Keywords Magnetorheological, Conical bearing, Conjugated heat transfer, Finite element analysis, Thermal management

List of symbols

$A_s(m^2)$	Static plug occupied area
$A_m(m^2)$	Moving plug plug-occupied area
$\vec{\boldsymbol{B}}$ (T)	Magnetic field flux density
C (m)	Clearance
Cp (J/(kg.K))	Specific heat capacity
D (m)	Journal major diameter
e (m)	Eccentricity
f	Friction coefficient
f^* :	Dimensionless friction coefficient
F_{or}(N)	Friction force
F^*_{fr}	Dimensionless friction force
F_x,F_y, F_z	Load components
h (m)	Film thickness
$\boldsymbol{H}$ (Am/m)	Magnetic field intensity
$\lvert\boldsymbol{H}\rvert$(Am/m)	Magnetic field value
$\boldsymbol{J}$ (A/m^2)	Current density
$\boldsymbol{J_e}$ (A/m^2)	Electrical current density

[1]Faculty of Mechanical Engineering, Shahrood University of Technology, Shahrood, Iran. [2]School of Mechanical Engineering, Eco-Friendly Smart Ship Parts Technology Innovation Center, Pusan National University, Busan, Republic of Korea. [3]Rolls-Royce University Technology Center, Pusan National University, Busan, Republic of Korea. ✉email: futurekim@pusan.ac.kr

K_f (W/(m.K))	Fluid thermal conductivity
K_s(W/(m.K))	Solid thermal conductivity
L (m)	Bearing length
L_s(m)	Solenoid length
P (Pa)	Pressure
P_a(Pa)	Ambient pressure
P_{max}(Pa)	Maximum pressure
T (K)	Temperature
R_j&R_b (m)	Journal and bearing major radius
S_o	Sommerfeld number
s	Ratio of plug surface
t^*	Maximum plug thickness ratio
$\overrightarrow{v}$ (m/s)	Velocity vector
W^*	Dimensionless bearing total load capacity
t (m)	Plug region thickness
W_R^*	Dimensionless radial load capacity
W_A^*	Dimensionless Axial load capacity

Greeks

α (°)	Cone angle
ε	Relative eccentricity
θ(°)	The angle from maximum clearance
θ_{Pmax}(°)	The angle of maximum pressure
μ(Pa.s)	Viscosity
μ_{pr} (N/A^2)	Magnetic permeability
μ_r	Magnetic relative permeability
ρ(kgm^{-3})	Density
σ (Ω·m)	Electrical conductivity
τ_y(Pa)	Yield stress
ϕ(°)	Attitude angle
φ(°)	The angle from maximum clearance
$\omega(rads^{-1})$	Rotational speed
η (Pa.s)	Virtual viscosity

Subscripts

b	Bearing
j	Journal

Superscript

*	Dimensionless variable

Elevated temperatures in lubricants play a pivotal role in the operational dynamics of bearings, serving as a key indicator of their performance. This paper delves into the intricate relationship between temperature fluctuations and bearing functionality, elucidating the mechanisms behind heat generation and its implications on lubrication. As temperature rises, the viscosity of lubricating oils decreases, potentially accelerating the onset of critical issues such as seizures. Moreover, thermal expansion alters bearing clearances, further influencing performance. Understanding the critical transition temperature of lubricants is paramount, as exceeding this threshold jeopardizes boundary lubrication, leading to rapid deterioration in bearing function. This paper investigates these phenomena and their consequences, with implications extending to oxidation and lubrication behaviors at extreme temperatures.

CFD simulation and thermal hydrodynamic lubrication (THL)

In recent decades, the thermal characteristics of bearings have been a subject of interest for numerous researchers[1–10]. Among the various research endeavors, particular emphasis has been placed on conical bearings due to their capability to simultaneously support axial and radial loads. In their study, Jeng and Yang[11] explored how thermal factors influence the performance characteristics of conical-cylindrical bearings. They analyzed this effect using two-dimensional (2D) and three-dimensional (3D) energy equations. Their research revealed that the performance of the bearings remains consistent across both 2D and 3D simulations when the piston rod speeds are low. Additionally, they delved into the effects of temperature on dual conical cylindrical bearings, examining the interplay among lubricant viscosity, pressure, and temperature to better understand their performance[12]. Tarawneh et al.[13] performed experiments aimed at measuring temperature fluctuations at different points within a stationary bearing subjected to heat sources incorporated into conical rollers. Similarly, Gao et al.[14] developed a quasi-static mechanical model of the bearing, tailored to certain testing conditions. This model enabled them to ascertain load distribution and kinematic parameters for double-row conical roller bearings.

The Reynolds and energy equations have been widely used to model thermo-hydrodynamic lubrication (THL). This approach faces many limitations, such as the inability to solve problems with complex geometry, turbulent flows, cavitation phenomenon, and modeling complex thermal conditions. Computational fluid dynamics (CFD) can overcome this disability. CFD uses complete momentum and energy equations to solve lubrication problems with geometrical complexity, thermal boundary conditions, and ordinary phenomena. Guo *et* al.[15] applied CFX-TASCflow to simulate a range of fixed geometric designs for fluid-film bearings and dampers. Uhkoetter et al.[16] presented a comprehensive three-dimensional multiphase-flow CFD approach, which accounted for cavitation and air entrainment in high-speed turbo-machinery journal bearings. Liu et al.[17] employed CFD utilizing the Navier–Stokes equation, alongside a fluid–structure interaction (FSI) approach. Their objective was to investigate the interplay between lubrication within the fluid film and the elastic dynamics of both the rotor and journal-bearing system. Deligant et al.[18] introduced a 3D CFD model to calculate power friction losses associated with turbocharger journal bearings, conducting computations under various oil entrance temperatures and rotational speeds. Papadopoulos et al.[19] conducted an extensive computational analysis of flow patterns and performance metrics in a dimpled parallel thrust bearing. Gengyuan et al.[20] applied three-dimensional computational fluid dynamics analysis to enhance the load-carrying capacity of water-lubricated journal bearings. Yang and Palazzolo[21] established a thermal-hydrodynamic lubrication model for circular bilayer porous bearings in polar coordinates, incorporating fluid pressure and heat transfer equations. They elucidated the fundamental sources of heat generation and its transfer mechanisms, with their findings highlighting that circumferential velocity plays a predominant role in determining temperature distribution.

Conjugated heat transfer

Unlike the traditional method (using the Reynolds equation), CFD solutions include many boundary conditions and geometries. In all the research mentioned above, researchers have simplified boundary conditions to reduce the complexity of heat transfer problems in lubrication problems. One of these simplifying assumptions does not consider the actual heat transfer conditions between the lubricating fluid and the solid bearing and journal, known as conjugated heat transfer (CHT). Guo et al.[22] mentioned the capability of CFD analysis in modeling the CHT effect, though only an initial simulation conducted on a long-bearing model was presented. Song and Gu[23] developed a three-dimensional CFD method to investigate journal bearings, taking into account CHT and cavitation effects. Their findings revealed that integrating CHT into the CFD approach yields more precise bearing load and temperature predictions than conventional Reynolds solutions or CFD models employing different thermal boundary conditions. Liu et al.[24] examined the temperature field, pressure field, and deformation of hydrostatic thrust bearings under various operating conditions. In these aforementioned studies, researchers embraced CHT as the complete thermal boundary condition, considering it a more realistic representation that aligns well with experimental findings.

Magnetorheological lubricant

In numerous bearing applications, conventional lubricants struggle to meet requirements such as precise control over film thickness, rapid response to shear stress changes, and compatibility with surrounding journal and bearing materials. To address these challenges, the use of smart lubricants like MR fluids has emerged as a promising strategy to enhance the load capacity of smart bearings, offering semi-active control capabilities and addressing the aforementioned limitations.Wang et al.[25] analyzed the dynamic properties of MR bearings using the Herschel-Bulkley model, comparing it with the Bingham model. Bompos and Nikolakopoulos[26] investigated the effects of lubrication with MR and nano-magnetorheological (NMR) fluids, finding that MR fluids exhibited higher yield stress than NMR fluids, whereas NMR fluids demonstrated higher viscosity. Wang et al.[27,28] explored how rotor-dynamic coefficients impact the stiffness and damping properties of controllable floating ring bearings utilizing MR fluid lubrication. Urreta et al.[29] focused on employing magnetic fluids as active lubricants to enhance the performance of hybrid journal bearings, particularly for high-precision machine tools. Sahu et al.[30] studied the behavior of magnetorheological (MR) lubricants within a hybrid slot-entry journal-bearing system (SEJBs) under journal misalignment and surface irregularities.

Considering the numerous applications of MRFs in industries and the undeniable role of heat transfer in the performance of these fluids, it is vital to investigate their heat transfer. Controlling heat transfer in fluids can reduce energy consumption depending on their application. Failure to control heat transfer in MRFs can reduce their performance. As the temperature increases in MRFs, their viscosity decreases and causes the fluid to malfunction. Also, it is essential to determine the operating temperature range of MRFs and the relationship between the rheological variables, such as viscosity and yield stress to the temperature. Among the literature, there are a few studies examining MRF heat transfer. Weiss et al. presented the first detailed description of the effect of temperature on the properties exhibited by electrorheological (ER) and magnetorheological (MR) fluids. Li et al.[31] investigated the rheological properties of MR fluids, MRF-132LD, under steady shear and oscillatory shear conditions for a range of operating temperatures from 20 to 60°C. Their results suggest that the MR fluid gets "thinner" with increasing temperatures. Wilson et al.[32] used hydro-mechanical analysis to represent MR damper behavior when subjected to large temperature perturbations. Bompos and Nikolakopoulos[33] investigated the dynamic characteristics of a journal bearing lubricated with magnetorheological fluids for various temperature and load conditions. Mitrouchev et al.[34] introduced a proper design for an MR damper within the emerging field of vibration control, taking heat transfer considerations into account. Wang et al.[35] explored the impact of temperature on the transmission characteristics of high-torque MR brakes by conducting a theoretical analysis of a disc brake, which considered the effects of viscous dissipation. Sahu and Sharma[36] developed a numerical simulation of a two-lobe hybrid slot-entry journal bearing lubricated with magnetorheological fluid. To enhance the realism of the operating conditions, they considered the influence of geometric imperfections

in the journal due to manufacturing inaccuracies and incorporated thermal effects. Using a rotary rheometer, Hemmatian et al.[47] experimentally investigated how temperature affects the rheological and viscoelastic properties of magnetorheological fluids (MRFs). Zschunke et al.[37] developed a relationship for the viscosity of MRFs considering the thermal effects. They showed how the fluid behavior could be modeled in CFD codes to design dampers or other applications. Sahin et al.[38] proposed a new yield stress model for magnetorheological grease based on an extended Herschel Bulkley constitutive relation, in which the shear yield stress is a magnetic field and temperature function. Bahiuddin et al.[39] presented constitutive models of magnetorheological fluids, which can predict the shear and dynamic yield stress depending on temperature. They modified the Herschel-Bulkley and power law model to consider the temperature for this aim. Haopeng Li et al.[40] investigated the effect of temperature on magnetorheological properties and its mechanisms. They proposed a novel constitutive model with temperature prediction by combining the Navier–Stokes and viscosity-temperature equations.

Scope of the present paper

The intricacies involved in examining heat transfer within MR fluids and the alterations in their properties with temperature have piqued the interest of researchers, motivating a significant emphasis on numerical solutions for addressing the associated challenges. However, a predominant trend in the existing literature has been the reliance on simplifying assumptions for computational convenience. Regrettably, these assumptions often lack physical fidelity, leading to less accurate results. Examples of such simplifications encompass treating heat transfer and flow boundary conditions and disregarding pertinent phenomena like plug regions within the solved domains. Furthermore, there are inherent complexities in modeling the heat transfer interactions between the bearing, journal, and fluid domains. To illustrate the distinctions between the presented work and similar studies, Table 1 provides a comparative summary. In a prior study by the authors[41], they investigated the performance of a conical hydrodynamic bearing with MR lubricant. A notable distinction between their earlier work and the present research is evident. In their previous work, the authors exclusively addressed the fluid and Maxwell domains, treating viscosity solely as a function of magnetic field and shear rate while expressing shear stress solely as a function of magnetic field. However, in the current study, the impact of temperature has been incorporated into the analysis. Consequently, viscosity is now influenced by magnetic intensity, shear rate, and temperature, with shear rate being considered a function of both magnetic field and temperature. Moreover, the investigation extends its scope by accounting for the effects of viscous dissipation and solving the energy equation. Conjugated heat transfer is also considered, evaluating the impact of actual boundary conditions on the bearing and journal.

In this study, a 3D simulation of a thermohydrodynamics (THD) conical bearing based on the CHT method using an MR lubricant in the presence of a magnetic field was developed. Cauchy momentum, Maxwell, and heat transfer equations are used to solve the flow field, magnetic field, and temperature distribution, respectively. Moreover, the rheological behavior of the MR fluid was modeled using the Bingham-Papanastasiou constitutive equation, with MRF-140CG from Lord Company chosen and employed as the lubricant.

The primary novel aspects of this research can be classified into the following categories:

1. Thermo-hydrodynamic modeling of MR conical bearings via the conjugate heat transfer method.
2. Detection and analysis of plug regions within the system in the presence of viscous dissipation.
3. Inclusion of viscous dissipation effects in the MRF bearings.
4. Consideration of magnetic field variations, resolved through the solution of Maxwell's equations and its effects on the heat transfer.
5. Thoroughly explore thermal boundary conditions around the shaft, bearing, and lubricants.

	MR bearing considerations				Governing equations	
Ref	Type	Core formation	Viscosity rel	Yield stress rel	Heat transfer	Flow
Laukiavich et al.[42]	Journal bearing	–	$\eta = Cte$	$\tau_y(H)$	–	Mass and momentum conservation equation
Gertzos et al.[43]	Journal bearing	Static and moving plug	$\eta = Cte$	$\tau_y = Cte$	–	Mass and momentum conservation equation
Urreta et al.[44]	Journal bearing	–	$\eta = K$	$\tau_y(H)$	–	Reynolds equation
Urreta et al.[29]	Journal bearing	–	$\eta = K$	$\tau_y(H)$	–	Reynolds equation
Sharma and Kumar[45]	Conical bearing	–	$\eta = (H, \dot{\gamma})$	$\tau_y(H)$	–	Reynolds equation
Sahu et al.[46]	Conical bearing	–	$\eta = (H, \dot{\gamma})$	$\tau_y(H)$	–	Reynolds equation
Sharma and Tomar[47]	Spherical bearing	–	$\eta = Cte$	$\tau_y(H)$	–	Reynolds equation
Vaziri et al.[41]	Conical bearing	Static and moving plug	$\eta(B, \dot{\gamma})$	$\tau_y(H)$	–	Cauchy momentum equations-Maxwell equations
Bompos et al.[33]	Journal Bearing	–	$\eta = Cte$	$\tau_y(T)$	Iterative procedure	Mass and momentum conservation equation
Sahu and Sharma[36]	Two-lobe hybrid slot-entry journal bearing	–	$\eta(T, \dot{\gamma})$	$\tau_y(H)$	Energy equation considering viscous dissipation	Reynolds equation
Present study	Conical bearing	Static and moving plug	$\eta(T, B, \dot{\gamma})$	$\tau_y(B, T)$	Energy equation considering viscous dissipation	Cauchy momentum equations-Maxwell equations

Table 1. Summary of MR Bearing papers.

6. Incorporation of MR fluid properties, including viscosity, yield stress, and heat transfer coefficient, as temperature and magnetic field functions.
7. A thorough analysis of how parameters like eccentricity, magnetic field strength, aspect ratio, and cone angle influence the heat transfer of conical MR bearings.
8. In-depth exploration of the functional properties of the bearing, including radial and circumferential load capacity, friction forces, pressure, and friction coefficients, all demonstrating sensitivity to changes in both magnetic field and temperature.

In this study, it is crucial to emphasize that all the above characteristics are intricately linked to magnetic field intensity and temperature interplay.

Simulation of the MRF conical bearing

Figure 1a illustrates the schematic of an MR conical bearing, and its solenoid arrangement, and Fig. 1b shows the conical bearing's coordinate system and eccentricity direction. In this setup, the shaft rotates while the bearing remains stationary. The solenoids are evenly distributed circumferentially around the bearing. A magnetic field is generated through these solenoids, inducing a current within them. These magnetic field lines traverse through

(a)

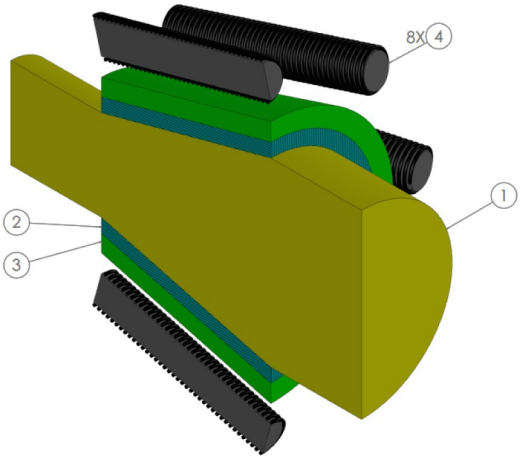

Item NO.	*Name*
1	Journal
2	MRF Domain
3	Bearing
4	Solenoid

(b)

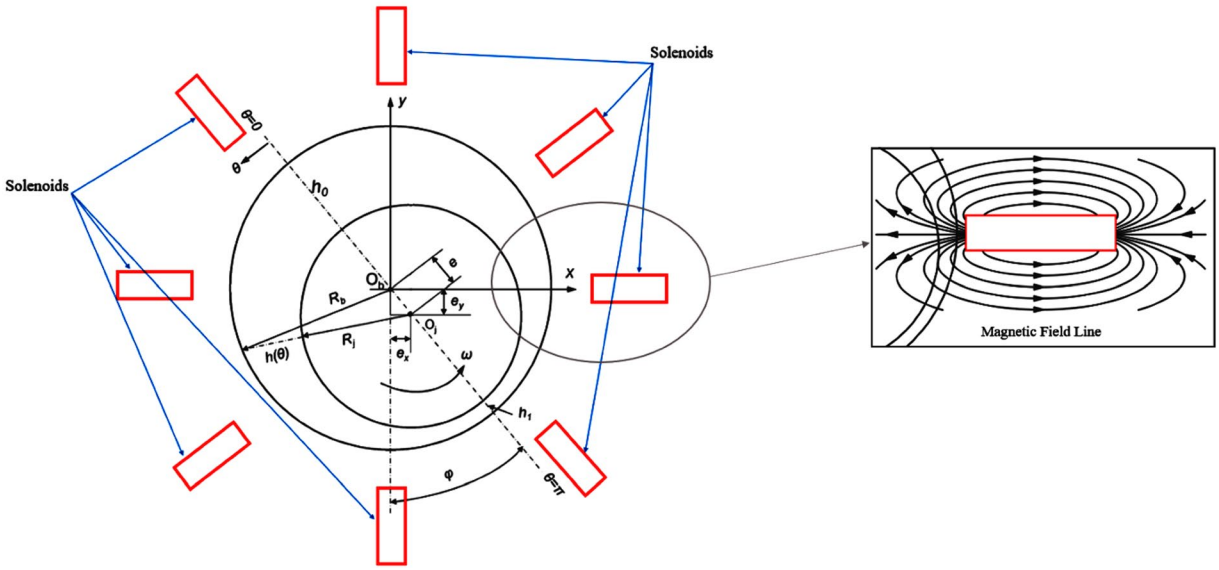

Fig. 1. Configuration of conical bearing and the magnetic field domain, including the (**a**) solenoid arrangement and (**b**) magnetic field lines and direction of eccentricity.

the fluid domain, subsequently altering the characteristics of the MR fluid. Understanding and specifying the direction of eccentricity is crucial in modeling and predicting the behavior of the system, particularly in fields like fluid dynamics, electromechanics, or engineering where solenoids and pressure profiles are relevant. In this paper, the eccentricity is in the direction of solenoid circumferential location.

Problem formulation and validation

Flow domain governing equations and boundary conditions

Because of the constraints of the Reynolds equation, a more precise formulation is necessary to effectively address lubrication challenges involving MR fluid. Cauchy's momentum equations are employed in this study to accurately resolve the flow field relations to achieve this goal. Although utilizing the Cauchy equations of motion instead of the Reynolds or modified Reynolds equations may escalate computational expenses, it also provides certain advantages that warrant their adoption.

The fundamental equations governing the flow of incompressible MR fluid consist of the continuity equation and the Cauchy momentum equations:

$$\nabla.\vec{V} = 0, \tag{1}$$

$$\rho\vec{V}.\nabla\vec{V} = -\nabla p + \nabla.\tilde{\tau} + \vec{F}. \tag{2}$$

Here, V represents the velocity vector, τ denotes the stress tensor, p signifies pressure, ρ stands for density, and F represents the external body force. No-slip boundary conditions were enforced at the walls. The bearing itself remained stationary while the journal rotated owing to angular velocity. Atmospheric pressure was assumed at the two ends of the bearing, allowing fluid to flow freely into and out of the bearing. A half-Sommerfeld boundary condition was applied to prevent sub-atmospheric pressure resulting from high angular velocity. As the Cauchy equation was utilized, the Reynolds boundary condition could not be applied. The solenoids were constructed from steel with linear properties, and their loads were determined by the current. These boundary conditions can be mathematically expressed as follows:

$$v_r\Big|_{r=r_j} = v_r\big|_{r=r_b} = v_\varphi\big|_{r=r_b} = v_z\Big|_{r=r_j} = v_z\big|_{r=r_b} = 0, \tag{3}$$

$$v_\varphi\Big|_{r=r_j} = r_j\omega,$$

$$p - p_a \geq 0, \;\; at \begin{cases} 0 \leq \varphi \leq 2\pi \\ z = 0, \; z = L \end{cases}, \tag{4}$$

in which v_r, v_φ and v_z are the radial, circumferential, and longitudinal velocities, respectively.

The following non-dimensional parameters have been considered for all bearing configurations with L/D ratios of 1/4, 1/2, 1, and 2 and a total clearance of $C = 50.2, 235\ \mu m$, and cone angle ranging from 0 to 15 degrees.

$$p^* = \frac{(p - p_a)C^2}{\mu\omega R_j^2}, \tag{5}$$

$$F_{fr}^* = \frac{F_{fr}C}{\mu\omega R_j^2 L}, \tag{6}$$

$$a = \frac{A_s + A_m}{2\pi R_b L}, \tag{7}$$

$$t^* = \mathrm{Max}\left\{\frac{t(\theta)}{h(\theta)}\right\}, \tag{8}$$

Conjugated heat transfer (CHT) governing equations and boundary conditions

Efficient bearing design hinges on effectively integrating heat transfer mechanisms within both fluids and solids, presenting a pivotal factor in minimizing heat losses. The temperature profile within a moving fluid can exhibit rapid variations, with the fluid closest to the solid surface mirroring its temperature while fluid further from the surface approaches the ambient fluid temperature. For a more comprehensive understanding of heat transfer, precise descriptions of heat transfer conditions, material properties, flow regimes, and geometric configurations are paramount.

Conjugate heat transfer analysis is employed to delve deeper into the interplay between fluid and solid, as they jointly facilitate heat transfer across domains. The Arbitrary Lagrangian–Eulerian Formulation (ALE) is a tool leveraged to seamlessly accommodate geometric changes within the fluid domain, enhancing the accuracy of these investigations.

Heat transfer in a solid. In most cases, heat transfer in solids, if only due to conduction, is described by Fourier's law, which defines the conductive heat flux proportional to the temperature gradient:

$$\nabla \cdot (k_s \nabla T) = 0 \tag{9}$$

where k_s is the thermal conductivity of the solid, and T is the temperature.

Heat transfer in a fluid. The energy equation is impacted by fluid motion in two significant ways:

1- Fluid motion inherently entails energy transfer, manifesting in the heat equation as convective terms. Convective or conductive heat transfer dominance depends on the fluid's thermal properties and the prevailing flow regime.
2- Viscous effects induced by fluid flow result in fluid heating, with a notable and substantial contribution from these effects in the case of viscous fluids.
3- Where C_p and k_f are Heat capacity and fluid thermal conductivity, respectively.

$$\rho C_p \vec{V} \cdot \nabla T - \nabla \cdot (k_f \nabla T) = \tilde{\tau} : \nabla \vec{V}. \tag{10}$$

In previous research, many investigators have resorted to simplifying boundary conditions due to the challenges involved in modeling thermal problems. However, in this study, a concerted effort has been made to employ comprehensive physical boundary conditions whenever possible. Utilizing physical boundary conditions enhances the accuracy of the solution results and brings them closer to real-world scenarios (Fig. 2). In bearing heat transfer problems, three primary boundary conditions have been commonly applied, as shown in Fig. 2: external convection, internal convection, and conduction.

Boundary A. Equations (11 and 12) show the normal heat flux and temperature continuity condition of the interface between lubricant and journal, where the conjugated heat transfer occurs.

$$k_J \left.\frac{\partial T_J}{\partial r}\right|_{r=r_J} = k_L \left.\frac{\partial T_L}{\partial r}\right|_{r=r_J}, \tag{11}$$

$$T_j(r = r_j) = T_L(r = r_j), \tag{12}$$

Boundary B. Equations (13 and 14) show the interface's normal heat flux and temperature continuity condition between lubricant and bearing.

$$k_B \left.\frac{\partial T_B}{\partial r}\right|_{r=r_B} = k_L \left.\frac{\partial T_L}{\partial r}\right|_{r=r_B}, \tag{13}$$

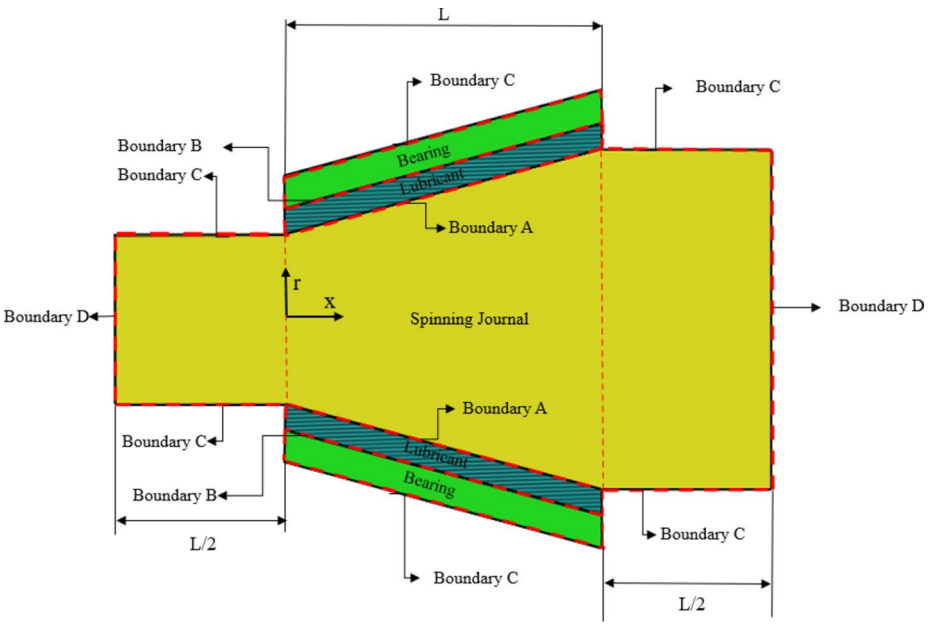

Fig. 2. Heat transfer boundary conditions.

$$T_B(r = r_B) = T_L(r = r_B), \tag{14}$$

Boundary C. Convection boundary conditions were applied on the outer surface of the bearing and journal that are in contact with air.

$$h_a(T - T_a) = -k_B \frac{\partial T_B}{\partial r}\bigg|_{r=r_B+t}. \tag{15}$$

Boundary D. Due to the considerable length of the journal versus its diameter, the adiabatic heat transfer is considered for the ends of the journal. This boundary condition reveals that the journal is sufficiently long, its temperature remains constant, and no heat is transferred to or from the surroundings.

$$\frac{\partial T_B}{\partial r}\bigg|_{x=-L} = \frac{\partial T_B}{\partial r}\bigg|_{x=-3L/2} = 0. \tag{16}$$

Amperes law and magnetic boundary conditions

In order to simulate the magnetic field, it is necessary to solve the Maxwell equations. The behavior of the magnetic field adheres to Ampere's law:

$$\nabla \times \vec{H} = \vec{J}. \tag{17}$$

Here, H represents the magnetic field intensity, while J denotes the electrical current density. The variable J includes the following definitions:

$$\vec{J} = \sigma \vec{E} + \vec{J}_e. \tag{18}$$

In this equation, J_e represents the externally generated current density vector, σ signifies the electrical conductivity, and E denotes the applied electrical field. As per the Maxwell equations, the magnetic field intensity is correlated with the magnetic flux through the B-H constitutive equation:

$$\vec{B} = \nabla \times A, \tag{19}$$

$$\vec{B} = \mu_{pr}\mu_r \vec{H}. \tag{20}$$

In this equation, μ_r represents the relative magnetic permeability, μ_r signifies the permeability of free space, and A stands for the magnetic vector potential. Additionally, the variations in the magnetic field can be accounted for by incorporating the permeability of the bearing and journal.

Employing solenoids offers a practical solution to address the issue of precisely applying the magnetic field to the MR fluid domain. Solenoids can be easily positioned, encircling the surface of the bearing, extending along its entire length, and producing a magnetic field perpendicular to the bearing surface (refer to Fig. 1). The arrangement of solenoids is designed to cover the entirety of the fluid domain comprehensively.

Both the solenoids and the bearing material are crafted from steel to ensure effective channeling and minimal dispersion of magnetic field lines. This choice of material provides advantageous tribological properties and assists in directing the magnetic field with minimal deviation. Notably, the shaft is constructed from nonmagnetic materials to prevent the magnetic flux from permeating through it.

After a thorough analysis of various solenoid configurations, it becomes evident that the most optimal arrangement comprises eight solenoids distributed circumferentially around the bearing, effectively spanning its entire length. In fact, for this purpose, 4, 6, 8, and 10 solenoids are positioned around the bearing in each scenario. Subsequently, the minimum and maximum magnetic field intensities are computed inside the bearing for the fluid domain using Maxwell's equations. For each solenoid, magnetic field lines are traced inside the bearing, influencing the magnetic field intensity at every point within the fluid domain. This assessment demonstrates the uniformity of the magnetic field. This layout minimizes the overlap and intensification of magnetic field lines while preserving the uniformity of the field. However, the variation between the minimum and maximum field intensities within the bearing gap remains below 4%. Moreover, this discrepancy has a negligible effect on the bearing's load capacity, resulting in a change of less than 1%. Consequently, the approach progresses by considering the average magnetic field intensity across different points within the fluid domains as the predominant intensity once the magnetic field has been resolved.

Table 2, presented below, explores how different numbers of solenoids influence magnetic field intensity under constant current conditions.

The setup includes a cover enclosing the magnetic circuit to maintain a consistent transverse field within the measuring gap. The outer surfaces of this cover were presumed to have zero magnetic potential. The load on the solenoid was described by the current density. Linear properties, specifically constant relative magnetic permeability (μ_{pr}), were attributed to the materials within the component. For instance, a value of 2000 for steel and 5 for the MRF was assigned to μ_{pr}. Both external and internal current density boundary conditions were considered for each solenoid.

Number of solenoids	B_{max}	B_{min}	$Error\left(\frac{B_{max}-B_{min}}{B_{max}} \times 100\right)$
4	60	0	100%
6	60	0	100%
8	61	59	4%
10	70	58	17%

Table 2. Effects of different numbers of solenoids.

MR lubricant properties

Utilizing magnetorheological fluids in industrial applications necessitates a profound comprehension of their properties and responses when subjected to external influences, including magnetic fields, temperature variations, and shear rates.

In this context, a thorough investigation of the steady shear behavior of a specific MR fluid (MRF-140CG, provided by Lord Co.) was carried out using the Anton Paar MCR501 Rheometer[48]. The tests covered a range of magnetic field strengths, spanning from 0 T to a maximum of 800 mT, with increments of 200 mT. Additionally, temperatures ranging from 20 to 50 °C, with increments of 10 °C, were explored. The ensuing results and findings are detailed in Fig. 3.

The unyielded regions generated by the Bingham plastic model present no concerns when $\dot{\gamma} > 0$. However, However, as the limit $\dot{\gamma} \to 0$ is approached. is approached, the apparent viscosity results in a singularity. Computational methods, such as the finite element method utilized in this investigation, are incapable of managing such singularities. To tackle this issue, these computational approaches can incorporate a continuation parameter. When selected appropriately, this parameter eases the solution process and yields nearly identical results to the ideal models. The primary objective of regularization schemes is to replace the discontinuous apparent viscosity as $\dot{\gamma} \to 0$ with an expression that remains bounded even for minimal $\dot{\gamma}$ values. Simultaneously, these schemes aim to approximate the rheological behavior effectively. One such scheme is the Bingham-Papanastasiou constitutive equation (Eq. 21), which transitions into the Bingham plastic model when the limit $m_p \to \infty$ is considered. When characterizing the rheological behavior of MRF-140CG, the Bingham model can adequately fit the shear stress-shear strain data.

$$\tau = \left(\mu_0(B,T) + \frac{\tau_y(B,T)}{\dot{\gamma}}[1-\exp(-m_p\dot{\gamma})]\right)\left(\nabla\vec{V} + (\nabla\vec{V})^T\right), \tag{21}$$

$$\eta(B,T,\dot{\gamma}) = \mu_0(B,T) + \frac{\tau_y(B,T)}{\dot{\gamma}}[1-\exp(-m_p\dot{\gamma})], \tag{22}$$

where η, μ_0, τ_y, m_p, and $\dot{\gamma}$ are the virtual viscosity, plastic viscosity, yield stress, model parameter, and shear rate, respectively.

A well-known relationship to correlate viscosity with temperature is Arrhenius[37,38].

$$\mu_0(B,T) = C_1 \exp\left(\frac{C_2(B)}{T}\right), \tag{23}$$

$$C_2(B) = \frac{E_a(B)}{R}, \tag{24}$$

$$E_a = aB + b, \tag{25}$$

where T is the temperature (K), C_1 is the viscosity level and considered as a constant for a given fluid, R is the universal gas constant, and E_a is the activation energy for flow. For a variation of the magnetic field strength at a constant shear, the slope $\partial\mu_0/\partial(1/T)$ curves for different field strengths are field-dependent. Thus, c_2 is a function of the applied magnetic field strength but independent of the shear rate[37].

Based on the shear stress–strain test results, it is evident that the yield stress is influenced by both the magnetic field strength and temperature, as described by the Arrhenius relationship proposed by Sahin et al.[38].

$$\tau_y = \nu B^{\alpha}\exp(-\zeta T). \tag{26}$$

Here, ν, α, and ζ represent constants, while T denotes the absolute temperature in Kelvin, which can be determined through regression analysis on experimental data.

The viscosity and yield stress data for different magnetic field strengths and temperatures are presented in Table 3.

The values of the constants in Eqs. (23–26) can be ascertained using the least squares regression technique by analyzing the experimental data depicted in Figs. 4 and 5.

The constants for Eqs. (23 and 26) can be obtained through curve fitting. As a result, the yield stress and plastic viscosity can be expressed as follows:

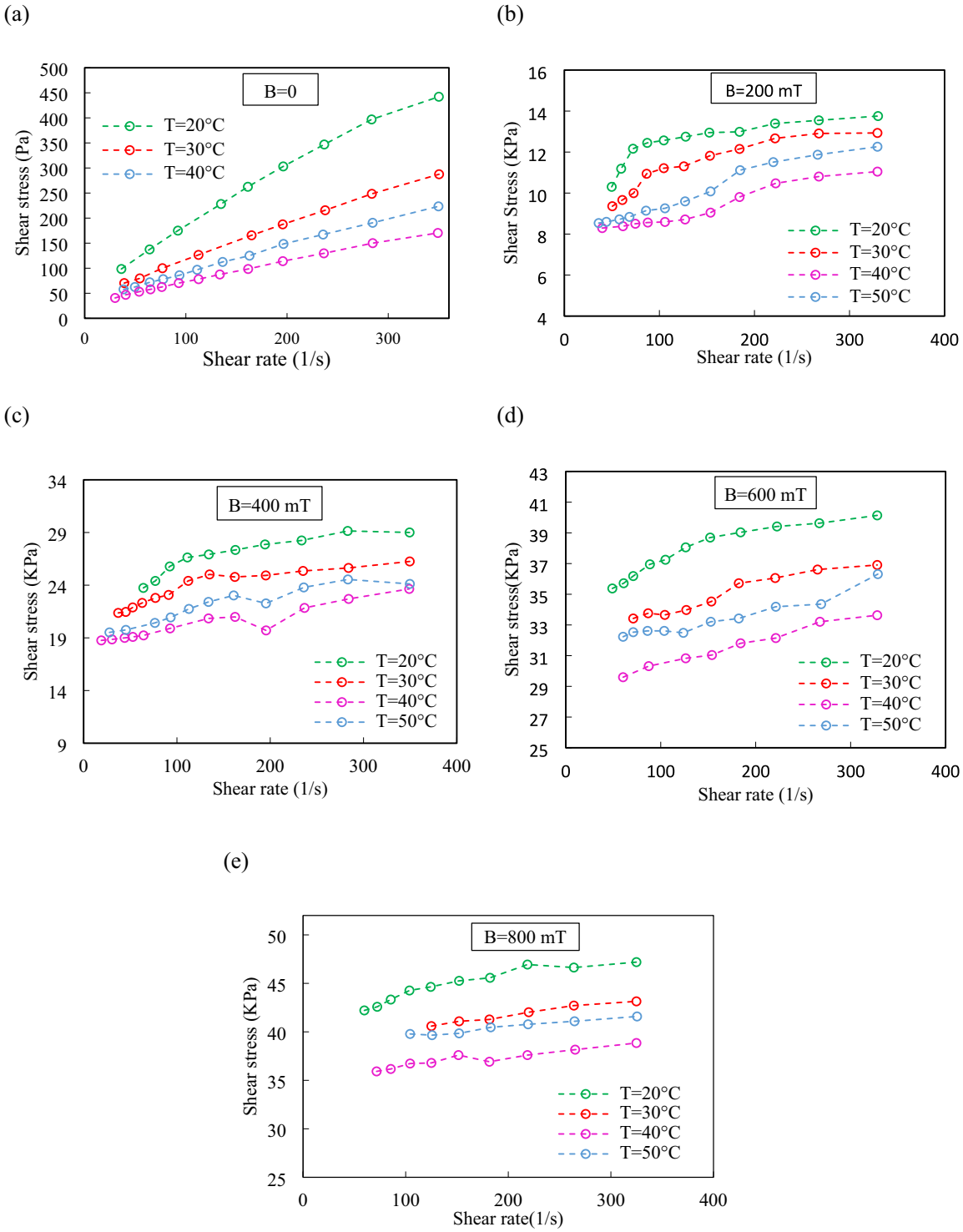

Fig. 3. Shear stress versus shear rate for different temperatures at (**a**) No magnetic field, (**b**) **B** = 200 mT, (**c**) **B** = 400 mT, (**d**) **B** = 600 mT, (**e**) **B** = 800 mT.

$$\tau_y = 58870B^{0.93}\exp(-0.0054T), \tag{27}$$

$$\mu_0(B,T) = 0.082\exp\left(\frac{-74.72B + 1647}{T}\right). \tag{28}$$

The fitted curves exhibit strong agreement with the experimental data. The constant values have minimal errors and have been optimized using a genetic algorithm.

Temperature (°C)	Magnetic field (mT)	Plastic viscosity (Pa.s)	Yield stress (KPa)
20	200	25.7	9.8
	400	17.5	22.8
	600	17.21	35.4
	800	19	41.55
30	200	17.1	9.7
	400	16.1	22.6
	600	14.1	34.3
	800	13.2	38.8
40	200	13.7	9.75
	400	15.9	20.7
	600	13.46	31.4
	800	10.5	37
50	200	11.6	8.66
	400	14.3	19.8
	600	15.23	30.4
	800	9.5	36.2

Table 3. Yield stress and viscosity for various magnetic fields and temperature based on bingham constitutive equation fitting.

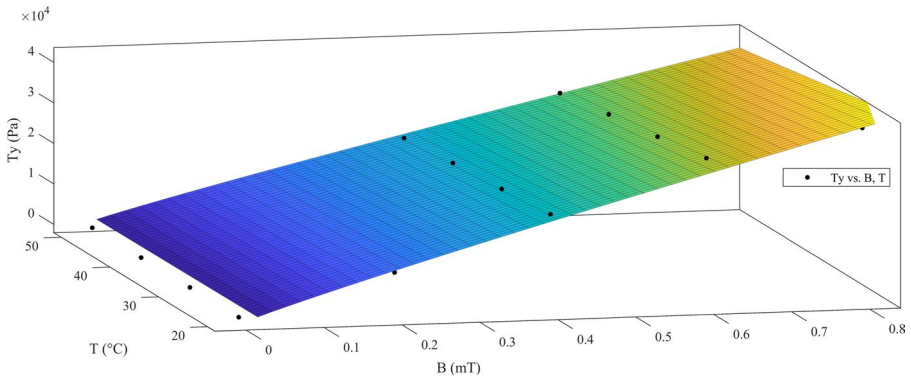

Fig. 4. The relationship between yield stress and both magnetic field strength and temperature (R-Square = 0.98).

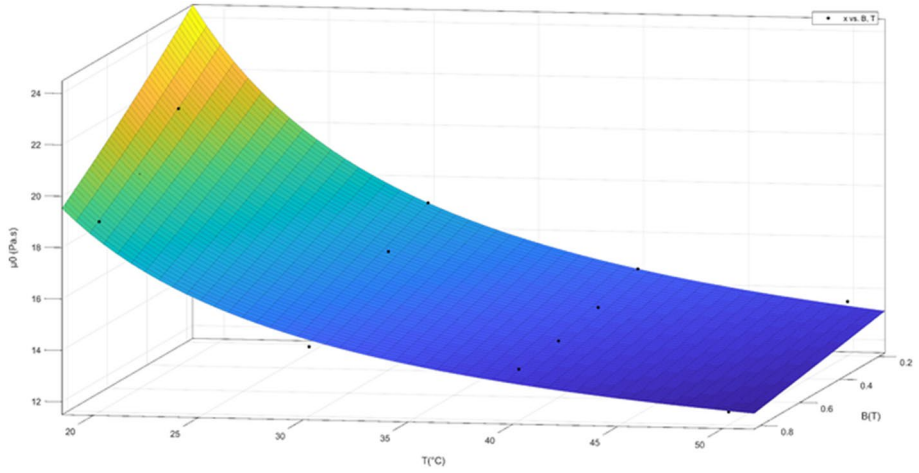

Fig. 5. Viscosity as a function of temperature and magnetic field (R-Square = 0.94).

Bearing performance characteristics

The critical aspect in addressing bearing lubrication challenges is the computation of the bearing's performance characteristics. Here, load carrying capacity is as follows:

$$W = \sqrt{W_R^2 + W_A^2}. \tag{29}$$

The load components, as well as the radial load-carrying capacities ($W_R = \sqrt{F_x^2 + F_y^2}$) and axial load-carrying capacities ($W_A = F_z$), can be expressed as follows:

$$F_x = \iint p \sin\varphi \cos\alpha \, d\varphi d\alpha, \tag{30}$$

$$F_y = \iint p \cos\varphi \cos\alpha \, d\varphi d\alpha, \tag{31}$$

$$F_z = \iint p \sin\alpha \, d\varphi d\alpha. \tag{32}$$

The friction load can be determined by integrating the wall shear stress across the surfaces of either the bearing or the journal, expressed as:

$$F_{fr} = \int \tau_w dA, \tag{33}$$

The friction coefficient can alternatively be ascertained by dividing the friction force by the total load capacity:

$$f = \frac{F_{fr}}{W}. \tag{34}$$

Numerical solution scheme and validation

Solution procedure

The flow, heat transfer, and magnetic field simulation within the MR conical bearing were effectively conducted using COMSOL Multiphysics software (version 5.6). An appropriate mesh discretized the solid, fluid, and magnetic domains. The steady-state solutions were obtained for the Cauchy momentum governing flow, the Maxwell equations governing the magnetic field, and the energy equations governing the lubricant and solid materials. The finite element method was applied to discretize these equations, and the resulting equation sets were solved using GMRES (generalized minimum residual) solvers for the magnetic, fluid, and heat transfer domains. A visual representation of the simulation process is depicted in Fig. 6.

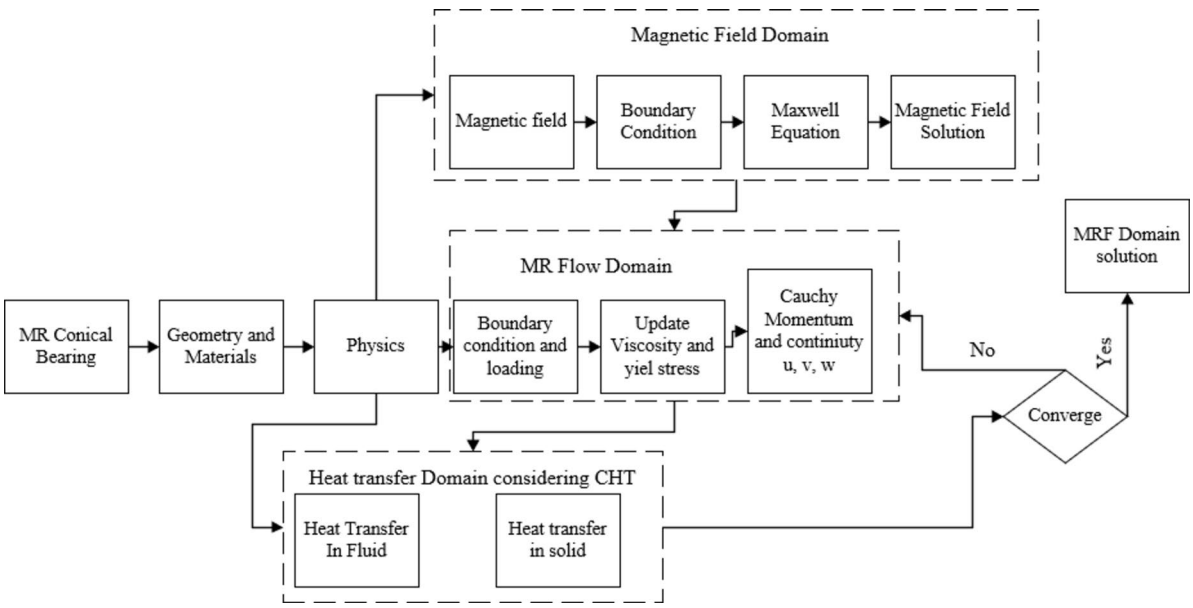

Fig. 6. Coupled simulation procedure block diagram.

Mesh sensitivity analysis

This section addresses the sensitivity of the results concerning the mesh size applied to both the fluid and solid domains. Mapped quadrilateral meshing has been predominantly employed to ensure precision. The grid study involved four different mesh configurations: extremely coarse, extra coarse, normal, and fine. The total load-carrying capacity of the bearing served as the pivotal parameter for this analysis. The maximum deviation of each mesh configuration from a reference grid was computed and visualized in Fig. 7. According to the figure, the deviation of the result of the normal grid relative to the fine mesh is negligible, so to decrease the numerical cost, the normal grid was selected for CFD simulations.

Model validation

Given the innovative nature of the findings presented in this article, encompassing the multiphysics domains, intricate geometric aspects, unique boundary conditions, and the limited availability of references concerning MR conical bearings, five distinct scenarios were employed to verify the results. Each scenario was used to validate the current model. Outcomes were rigorously compared with existing analytical, numerical, and experimental data, comprehensively evaluating the validity of the 3D simulation for the magnetic field, flow, and heat transfer characteristics.

The scenarios are as follows:

1. Validation of the non-dimensional pressure distribution for a Newtonian journal bearing was conducted based on studies by Gertzos et al.[43] and Wada et al.[49]. This validation assumed a cone angle of zero and did not consider yield stress. Figure 8 demonstrates that our results deviate by approximately 2% compared to the findings of Gertzos and Wada.
2. Validation of the non-dimensional pressure distribution for a Bingham journal bearing was performed based on the studies by Gertzos et al.[43] and Wada et al.[49]. This validation also assumed a cone angle of zero, with a constant yield stress considered. Figure 9 indicates that the maximum deviation between our CFD results and experimental data is approximately 2%.
3. Validation of the load capacity for the MRF bearing was carried out based on the studies by Urreta et al.[44] and Sharma and Kumar[45]. This validation set the cone angle to zero, treating the yield stress as a magnetic intensity function. Figure 10 shows that our results exhibit a maximum deviation of 3% compared to Sharma and 8% with Urreta.
4. Validation of the radial and axial load capacity for the conical bearing followed studies by Stout and Rowe[50] and Sharma and Kumar[45]. In this validation, yield stress was not taken into account. The maximum deviation between the results presented in Fig. 11 and Stout and Rowe[50] is roughly 5%, and with Sharma and Kumar[45], it is around 2%.
5. Validation of the temperature distribution in the journal bearing, considering conjugate heat transfer in line with studies by Li et al.[51] and Ferron et al.[52]. The heat transfer validation was conducted for a finite journal bearing, utilizing the Newtonian fluid referred to in Li's article. Figures 12 and 13 show that the results reveal a maximum deviation of approximately 4% with Ferron et al.[52] and 3% with Li et al.[51].

Based on the analysis of the referenced studies and the results presented here, it is evident that the obtained results demonstrate strong concordance with the findings of the validation studies.

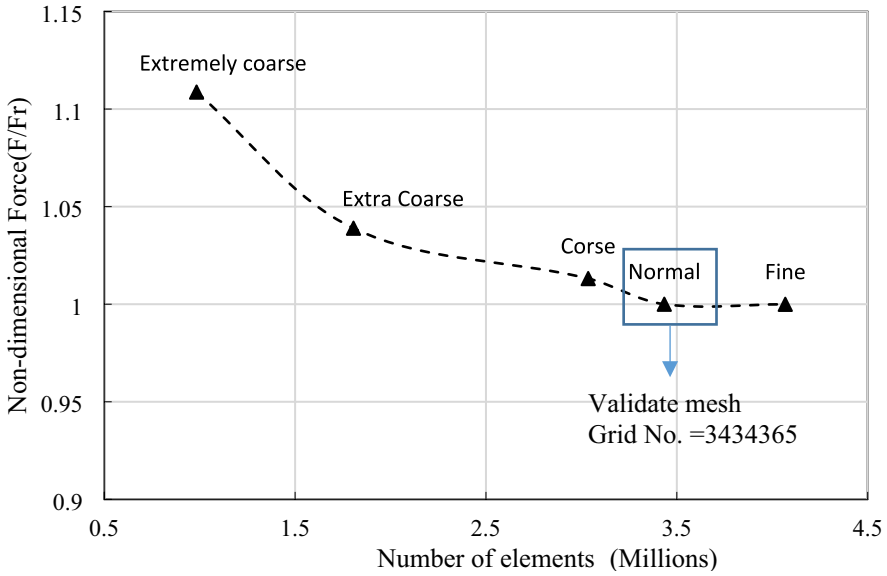

Fig. 7. The diagram of dimensionless force versus the number of elements.

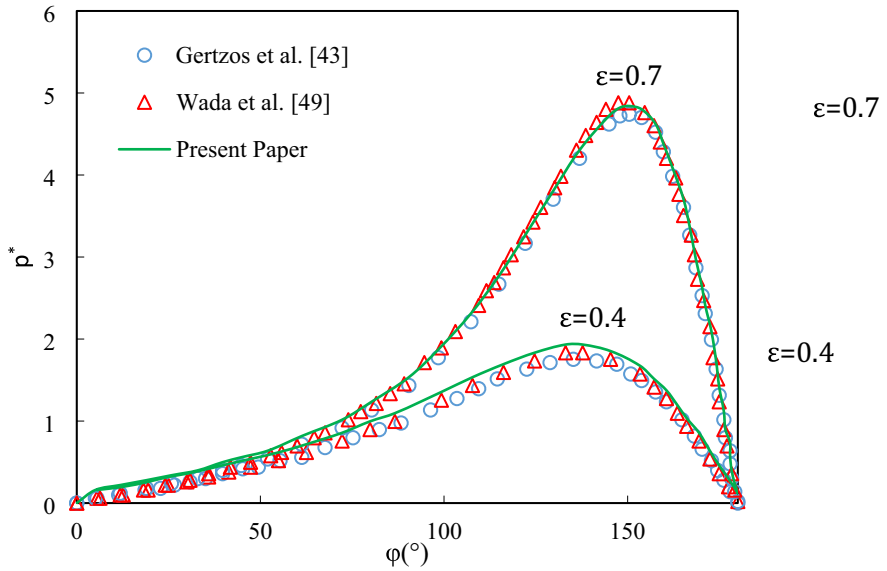

Fig. 8. Validation of the non-dimensional pressure distribution for Newtonian journal bearing according to Gertzos et al.[43] and Wada et al.[49].

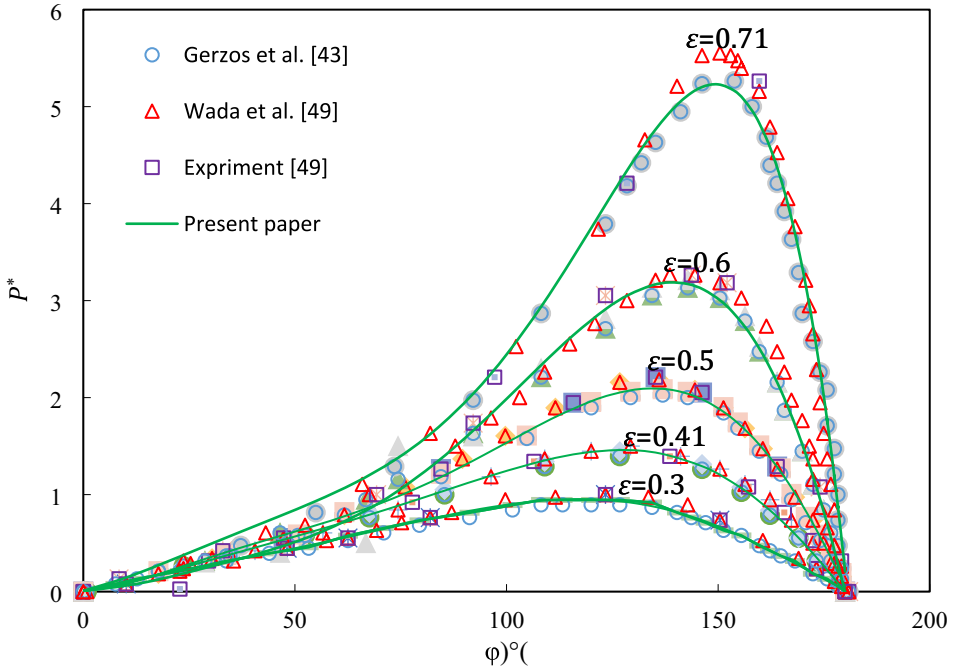

Fig. 9. Validation of the non-dimensional pressure distribution for Bingham journal bearing according to the Gertzos et al.[43] and Wada et al.[49].

Results and discussion

In the present study, the combined effects of the nonlinear behavior of MR fluid in the presence of magnetic fields and conjugate heat transfer have been investigated. The Bingham-Papanastasiou constitutive equation has been employed to model MR fluid behavior using COMSOL Multiphysics. This section explores the influence of various parameters, including magnetic field intensity, viscous dissipation, aspect ratio, eccentricity, and cone angle, on the flow and heat transfer domains. This paper presents results in a dimensionless format commonly used in various bearing scenarios to facilitate comparisons with other cases.

Table 4 outlines the bearing geometry, MR fluid properties, and operational parameters:

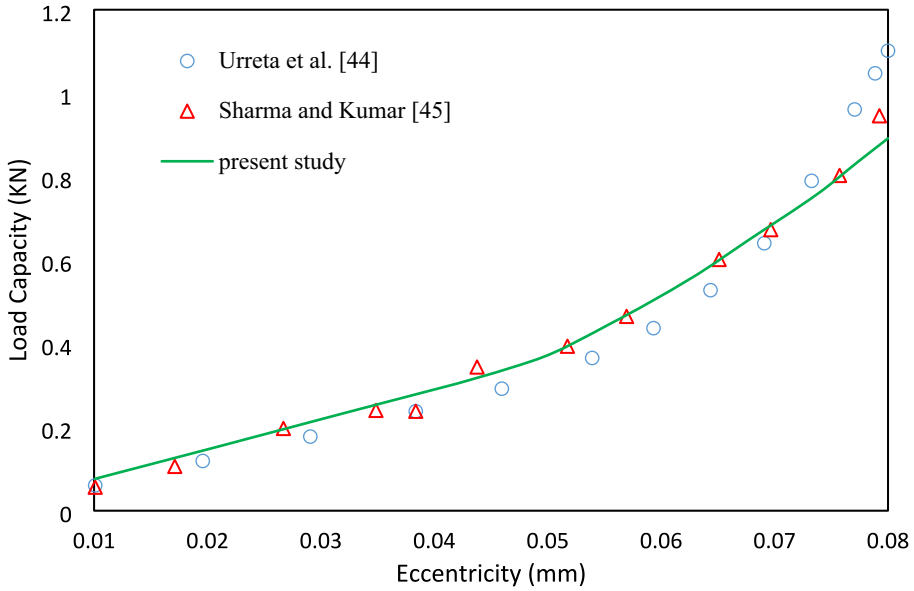

Fig. 10. Validation of the load capacity for MRF bearing according to Urreta et al.[44] and Sharma and Kumar[45].

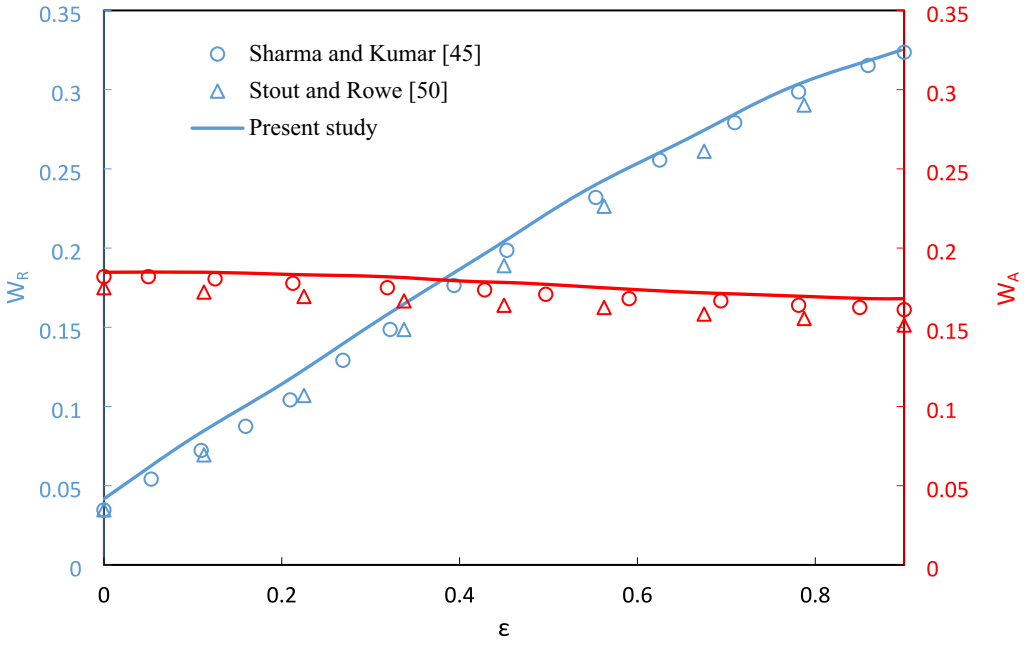

Fig. 11. Validation of the radial and axial load capacity for conical bearing according to Stout and Rowe[50] and Sharma and Kumar[45].

Thermal analysis

In reaction to a magnetic field, specialized smart fluids, known as magnetorheological (MR) fluids alter their rheological (flow and deformation) characteristics, including viscosity. Monitoring and maintaining lubricant temperatures regularly is crucial to prevent overheating, early wear, and lubricant breakdown, all of which can adversely affect bearing performance and lifespan. Here is a deeper look at the MR fluid's thermal behavior:

The MR fluid undergoes shear stresses that produce heat as it moves through the small gaps between the bearing components. This heat is a result of the fluid encountering viscous resistance. The areas where the fluid experiences the most shear and friction generally have higher temperatures. As shown in Fig. 14, the temperature increased by increasing the angular velocity and magnetic field, but the angular velocity contribution is more significant than the magnetic field. The angle of maximum temperature decreases due to increasing the angular

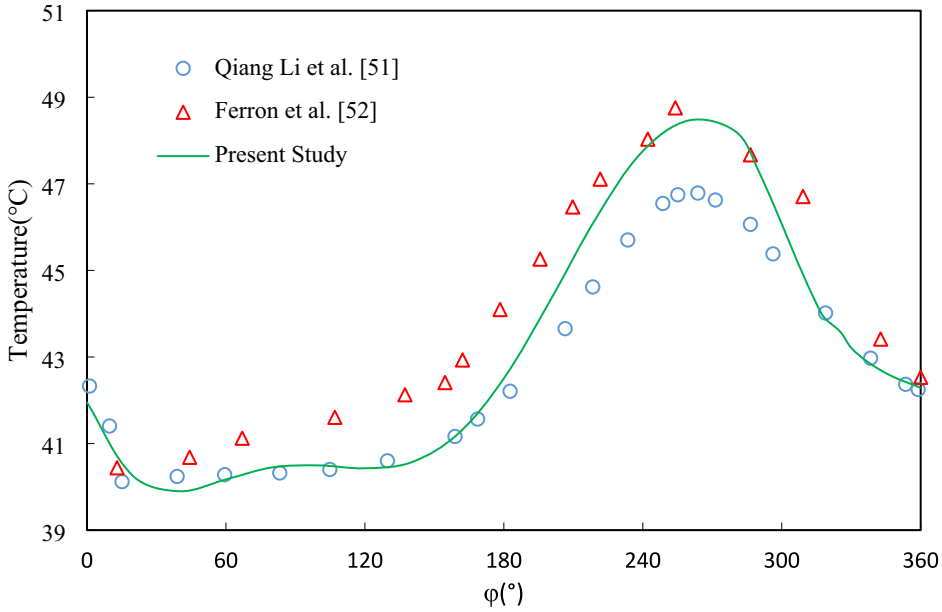

Fig. 12. Validation of the temperature distribution of journal bearing considering conjugated heat transfer according to Li et al.[51] and Ferron et al.[52].

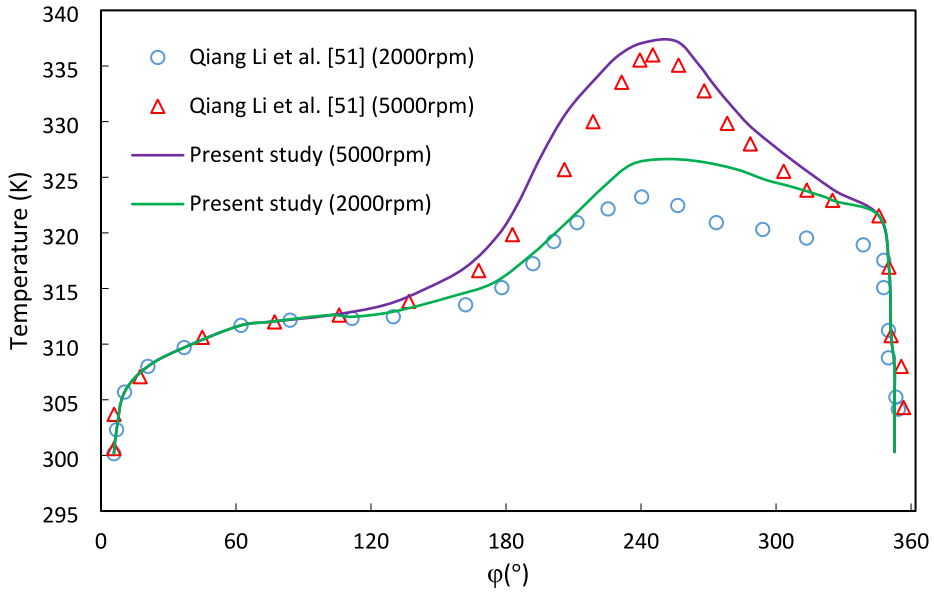

Fig. 13. Validation of the temperature distribution of journal bearing considering conjugated heat transfer according to Li et al.[51] at different angular velocities.

velocity and remains constant by increasing the magnetic field. For example, the maximum temperature angles for angular velocities of 40, 60 and 80 are 200°, 188° and 181°, respectively.

Higher angular velocities can lead to steeper temperature gradients as more heat is generated, and there may be less time for heat to travel axially and dissipate, potentially leading to higher axial temperature gradients. Figure 15 shows the axial distribution of temperature in solid and fluid domains. The maximum temperature occurs at the lowest film thicknesses of MR lubricant.

In magnetic bearing systems, eccentricity describes the deviation of the shaft from its central axis. The temperature distribution of MR bearings can be affected by eccentricity in several ways. Eccentricity may cause the temperature distribution inside the MR bearing to be out of balance. The greater eccentricity of the bearing results in higher frictional forces and temperatures in those areas. In contrast, temperatures are lower in areas with lower eccentricity. The performance and lifespan of the bearing may be impacted by these temperature gradients' potential to cause thermal stresses inside the bearing. Figure 16 shows the circumferential temperature

Parameter	Notation	Values
Density	(ρ)	3.64 g/cm^3
Clearance	(C)	50.2 µm
Bearing major radius	(R_b)	25 mm
Journal major radius	(R_j)	$R_b - C$
Aspect ratio	($\lambda = L_b/D$)	1/4, 1/2, 1, 2
Bearing length	(L_b)	λ × D
Journal length	(L_j)	3 × L_b
Eccentricity ratio	(ε)	0.4–0.9
Journal speed	(ω)	40, 60, 80,120 rpm
Cone angle	(α)	5 °, 10 °, 15 °
Solenoid length	(L_s)	λ × D
Convective heat transfer coeff	h	8 W/(m^2.K)
Conduction heat transfer coeff	K_{steel}	25 W/(m.K)
Solid specific heat	$C_{p,\ steel}$	460 J/(kg.K)

Table 4. Bearing geometry, MR fluid characteristics, and operating parameters.

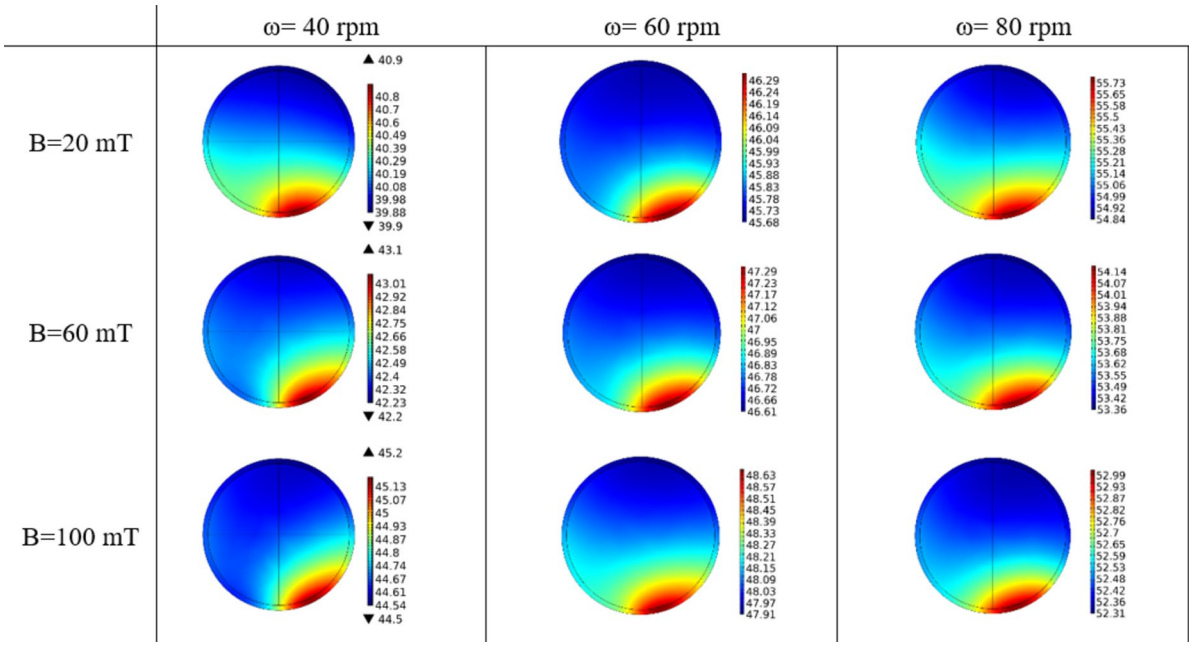

Fig. 14. Radial Temperature distribution versus magnetic field intensity and angular velocity at a middle section of the solid and fluid domain $\varepsilon = 0.7$, $\alpha = 10°$, and $\lambda = 1$.

distribution of MR lubricant. The temperature in regions near the minimum thickness of the lubricant (at the graph's start and end) is elevated compared to other areas. As evident, raising the eccentricity from 0.4 to 0.9 results in a 20% increase in the maximum temperature.

Enhancing the intensity of the magnetic field can result in an elevation of temperature within the MR fluid. This temperature increase is commonly linked to the activation of the MR effect, wherein the alignment of magnetic particles in the fluid generates heat due to friction and energy dissipation. With the amplification of magnetic field intensity, there is typically a concurrent increase in the viscosity of MR fluids. This alteration in viscosity can impact the fluid's flow characteristics and heat dissipation, thereby influencing the temperature distribution. Variations in magnetic field strength can introduce non-uniform temperature gradients within the MR fluid, wherein regions exposed to higher field intensities may undergo more substantial temperature fluctuations than areas with weaker magnetic fields. In practical applications, effectively managing the temperature elevation induced by the magnetic field becomes imperative. Implementing cooling systems is necessary to disperse excess heat and uphold a consistent and stable temperature distribution. Figure 17 shows the variation of temperature versus magnetic field intensity. Here, increasing the magnetic field intensity from 20 to 100 results in an approximately 11% increase in the maximum temperature rise. The effects of angular velocity on MR temperature in bearings are complex and depend on various factors.

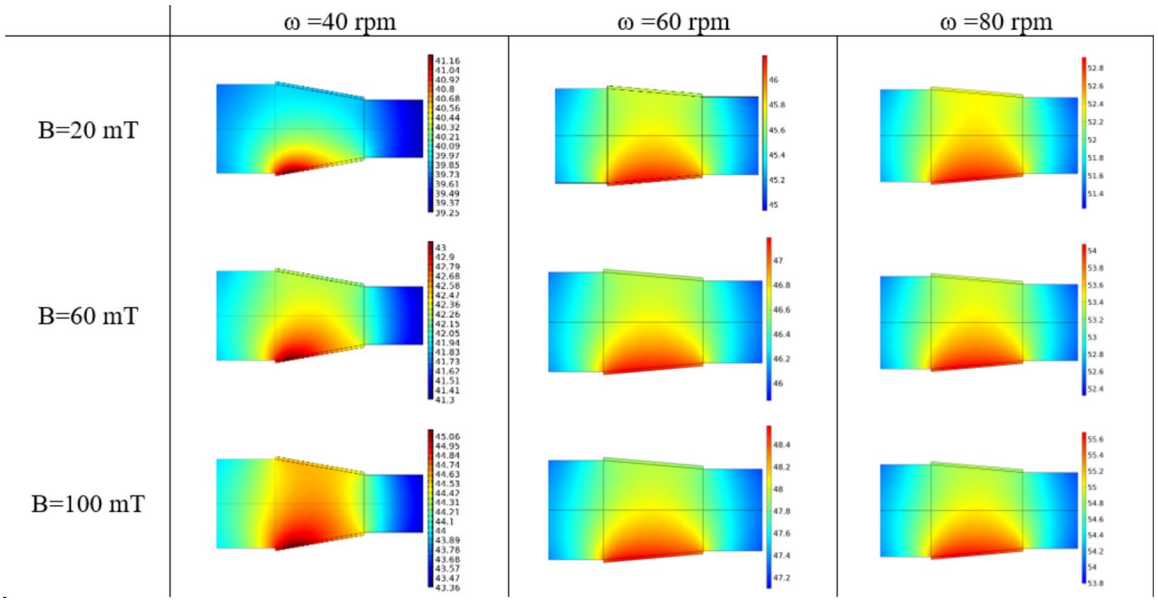

Fig. 15. Axial temperature distribution versus magnetic field intensity and angular velocity of the journal and bearing $\varepsilon = 0.7$, $\alpha = 10°$, and $\lambda = 1$.

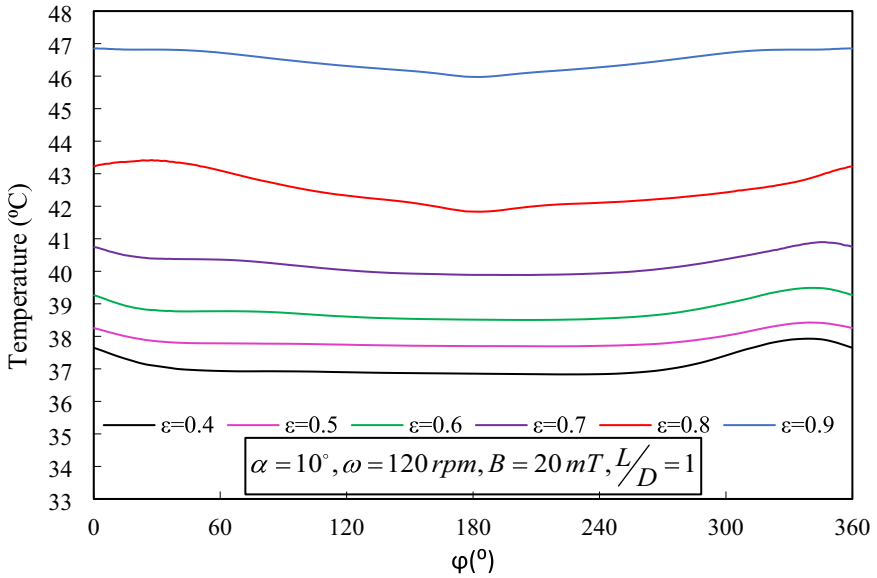

Fig. 16. Circumferential temperature distribution for different eccentricities.

- Higher angular velocities can induce greater friction and shear forces within the bearing, potentially causing the temperature of the MR fluid to increase. This rise in temperature is commonly linked to the mechanical energy generated due to the relative movement between the various components of the bearing.
- Variations in angular velocity can impact the viscosity of the MR fluid. In specific scenarios, increased angular velocity can reduce viscosity due to shear-thinning behavior. In contrast, in other instances, it may increase viscosity because of the alignment of magnetic particles.
- The angular velocity can impact the heat dissipation within the bearing system. Higher angular velocities may lead to more rapid heat generation within the MR fluid.
- The angular velocity can affect the dissipation of heat within the bearing system. Increased angular velocities can accelerate the generation of heat within the MR fluid.
- The angular velocity can influence the activation of the MR effect, which entails the alignment of magnetic particles in reaction to a magnetic field. In certain situations, elevated angular velocities can intensify the alignment of magnetic particles, resulting in alterations to the fluid's rheological characteristics and, consequently, its temperature behavior.

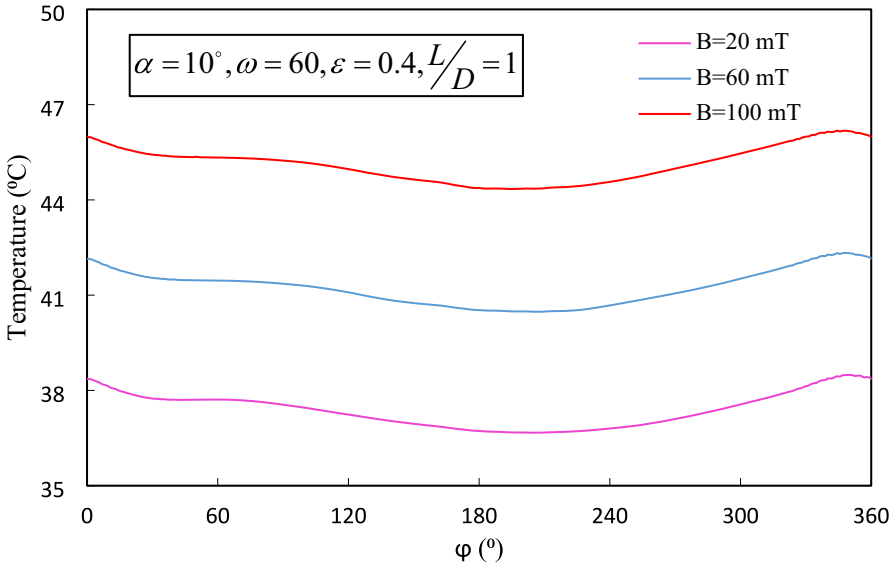

Fig. 17. Circumferential temperature distribution for different magnetic field intensity.

Figure 18 shows the temperature distribution of MR lubricant for different angular velocities. The effects of angular velocity on viscous dissipation are more significant. The cone angle determines the temperature distribution within a conical MR bearing. A steeper cone angle may result in higher contact pressures and shear forces, leading to increased heat generation due to friction between bearing components and within the MR fluid. A shallower cone angle may provide better lubrication between the bearing surfaces, reducing friction and heat generation, while a steeper cone angle might lead to less effective lubrication. In summary, an optimal cone angle design may be necessary to balance heat generation, lubrication effectiveness, and temperature control to ensure stable and reliable operation. Figure 19 shows the temperature distribution of MR conical bearing for different cone angles. It has been demonstrated that bearing temperatures may increase due to steeper cone angles.

Pressure distribution

This section delves into the analysis of pressure variation, considering factors such as cone angle, eccentricity, viscous dissipation, and angular velocity. The half-Sommerfeld boundary condition was employed to better reflect the problem's physical aspects. When the film pressure decreases to atmospheric pressure, it leads to film cavitation, primarily driven by radial loads or high rotational speeds. High-speed, high-pressure, or extreme load conditions are more likely to induce cavitation. In contrast, cavitation may be less likely to occur under

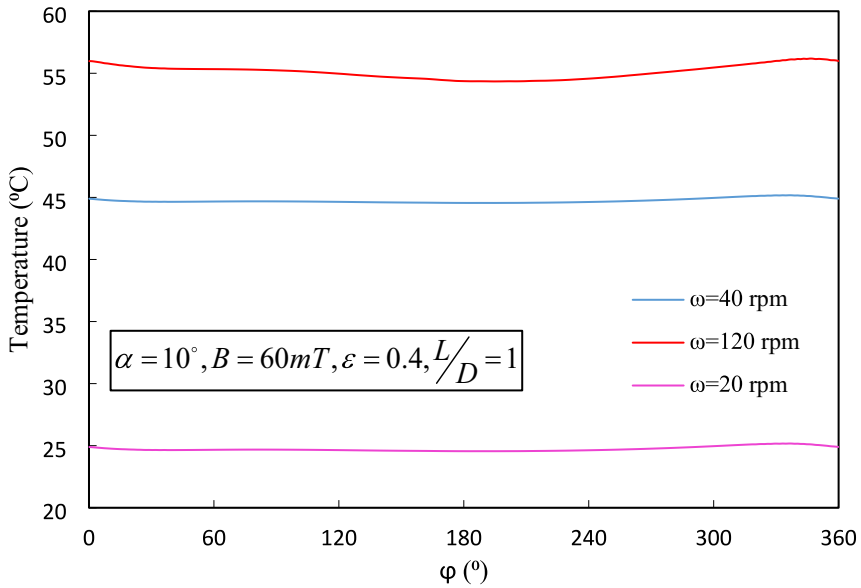

Fig. 18. Circumferential temperature distribution for different angular velocity.

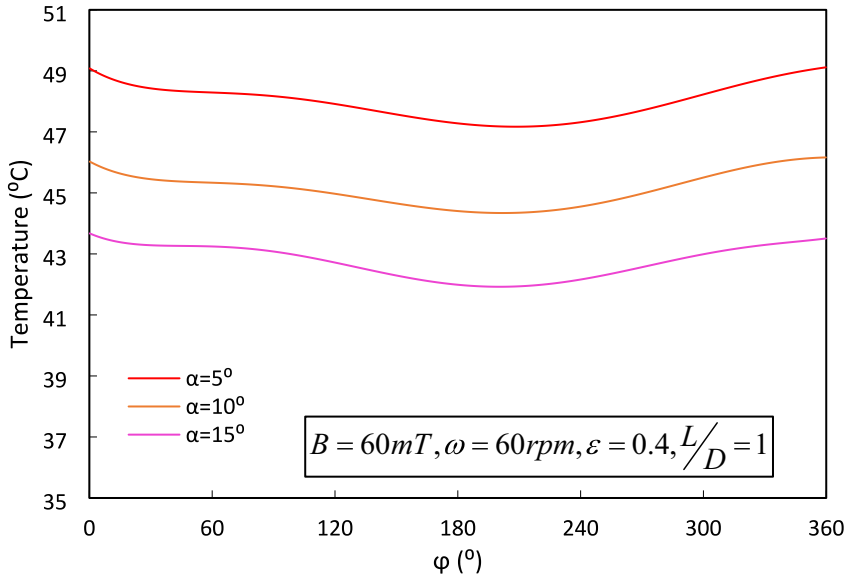

Fig. 19. Circumferential temperature distribution for different cone angle.

low-pressure and low-speed conditions. Also, the type of lubricant used can influence cavitation. Some lubricants are more prone to cavitation than others. Lubricants with low viscosity are more likely to experience cavitation compared to high-viscosity lubricants. Higher temperatures and pressures can mitigate cavitation, while lower temperatures and pressures can promote it.

Consequently, cavitation is not considered in this study. Many previous studies have opted for the Reynolds boundary condition. The direct solution of the Cauchy momentum equation is warranted in this context, given the utilization of MR fluids. However, it is essential to note that no modified Reynolds equation has been developed to apply the Reynolds boundary condition.

Figure 20 depicts the contour of pressure distribution for varying cone angles and eccentricity. It is evident that when both eccentricity and cone angle increase, the point of maximum pressure shifts away from the point of maximum clearance. Additionally, a higher cone angle decreases pressure, whereas an increase in eccentricity leads to elevated pressure levels.

Viscous dissipation generates heat within the MR fluid due to the shearing of its particles as it flows within the bearing. This heat can cause a temperature rise in the bearing system. Elevated temperatures can impact the viscosity and rheological properties of the MR fluid. Increasing fluid viscosity may lead to higher pressure in some bearing areas. If the temperature rise is significant, it might reduce the load-carrying capacity of the bearing, potentially causing areas of higher pressure, which could result in localized wear or other issues. Figure 21 investigates the impact of viscous dissipation on the pressure distribution within an MR conical bearing. As demonstrated, the inclusion of viscous dissipation results in a reduction in pressure. For instance, in the case of $\varepsilon = 0.9$, the maximum pressure experiences a decrease of approximately 50 percent when accounting for viscous dissipation.

The angular velocity of a bearing can have several effects on viscous dissipation. Higher angular velocity leads to an increase in the shear forces within the bearing. This increased shear can intensify the frictional forces and heat generation due to viscous dissipation. As previously noted, elevated temperatures can lead to a reduction in pressure. It is essential to emphasize that, in the absence of viscous dissipation, an increase in angular velocity results in elevated pressure. However, when accounting for viscous dissipation and subsequently increasing its magnitude, the pressure experiences a decrease. Figure 22 illustrates the influence of angular velocity and viscous dissipation on the pressure distribution of MR Conical bearing. Comparatively, the temperature variation is significantly more significant in the absence of viscous dissipation as opposed to when viscous dissipation is considered.

Yield stress variation

Viscous dissipation generates heat within MR fluids due to the shearing of their constituent particles. This heat can result in a rise in the temperature of the MR fluid. In the context of this research, it is essential to note that the yield stress of MR fluids is influenced by both temperature and magnetic field strength, as described by Eq. (15). Increasing temperature can reduce the yield stress, rendering the fluid less deformation-resistant. Furthermore, the yield stress exhibits a high degree of sensitivity to the intensity of an applied magnetic field. When a magnetic field is introduced, the yield stress generally experiences an increase, signifying an enhanced resistance to deformation or flow when subjected to a magnetic field. As the strength of the magnetic field intensifies, the yield stress proportionally increases, and this relationship is harnessed to govern and modulate the rheological properties of MR fluids in various engineering applications. The magnetic field serves as a valuable tool for the precise control and adjustment of the yield stress of MR materials, offering a versatile means to tailor material

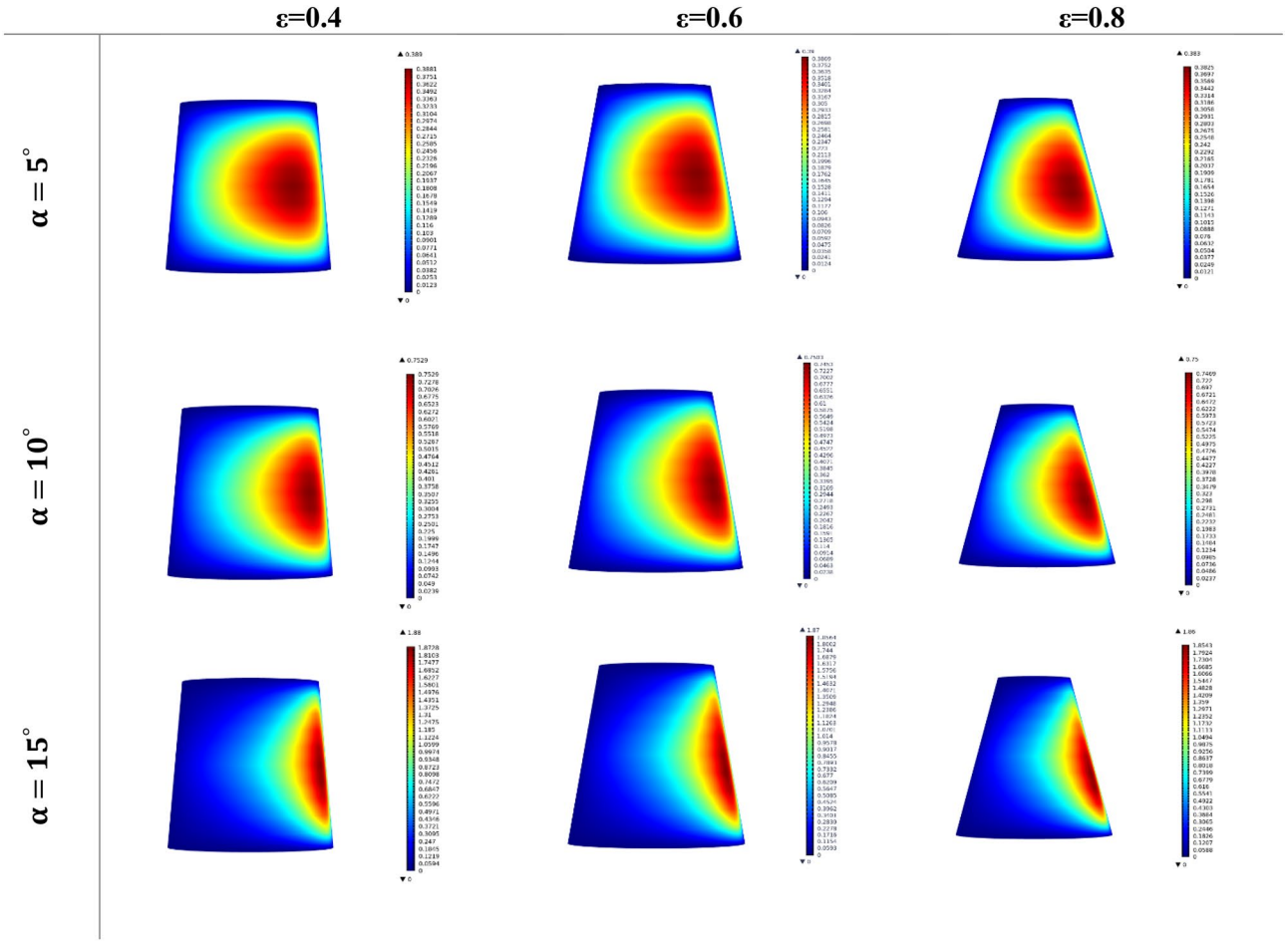

Fig. 20. Pressure distribution according to the eccentricity and cone angle for l/d = 1, b = 60 mt, ω = 60 rpm.

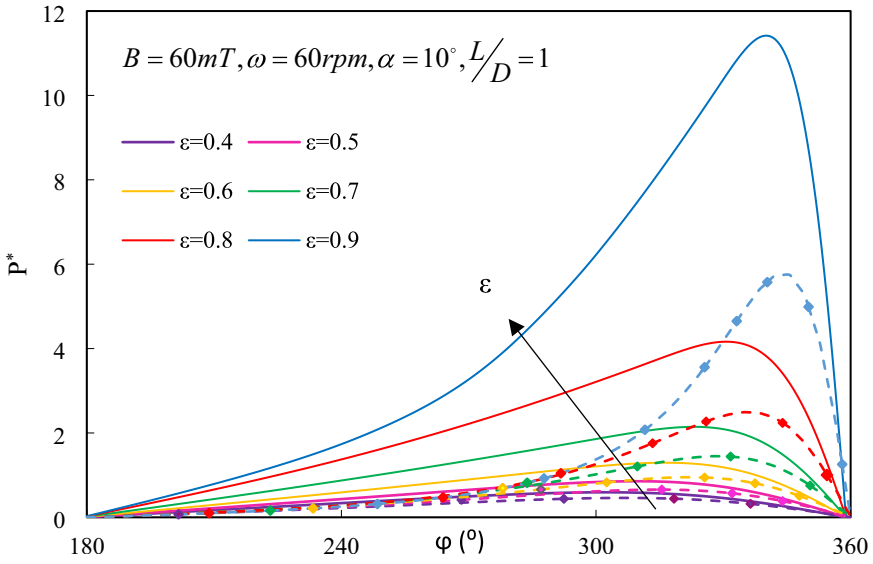

Fig. 21. Dimensionless pressure distribution versus angle of maximum clearance (ϕ) at various eccentricities. Dashed lines represent outcomes when considering viscous dissipation, while solid lines pertain to results when viscous dissipation is not considered.

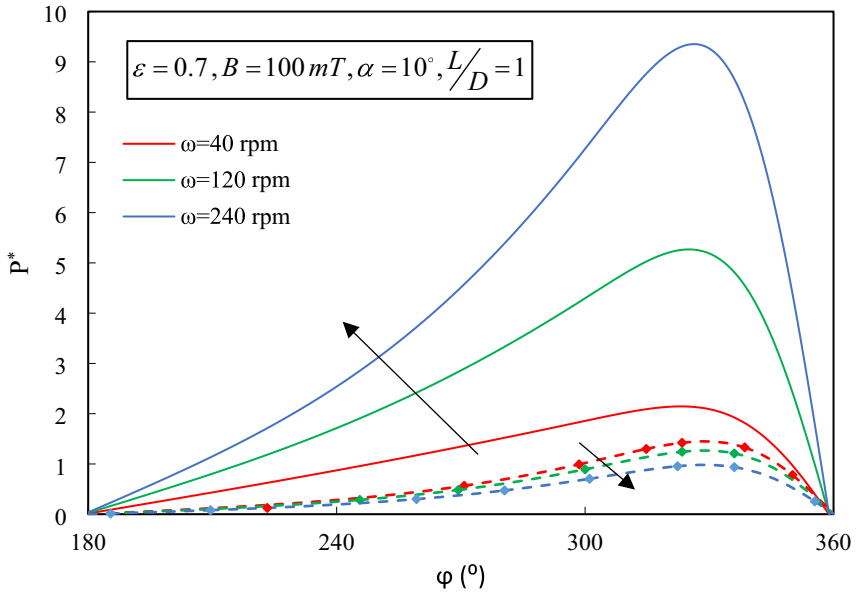

Fig. 22. Dimensionless pressure distribution versus angle of maximum clearance (ϕ) for various angular velocities. Dashed lines represent outcomes when considering viscous dissipation, while solid lines pertain to results when viscous dissipation is not considered.

characteristics in alignment with specific engineering requisites. Figures 23, 24 and 25 illustrate the changes in yield stress concerning eccentricity, temperature, and magnetic field. These visual representations reveal that an increase in eccentricity correlates with a temperature rise, resulting in a subsequent decrease in yield stress.

Additionally, when the magnetic field strength reaches 60 mT and 100 mT, the yield stress is notably more significant, measuring 62% and 75% higher than 20 mT, respectively. When the yield stress is not influenced by temperature, it experiences an increase, as shown in Fig. 26. For instance, at B = 100 mT, the yield stress in the presence of viscous dissipation is 28% lower than when viscous dissipation is absent.

Plug regions

In applying MR fluids, anticipating plug formation regions is a significant challenge. The plug region is typically defined as an area where the shear stress is lower than the yield stress, causing the fluid to behave like a semi-solid

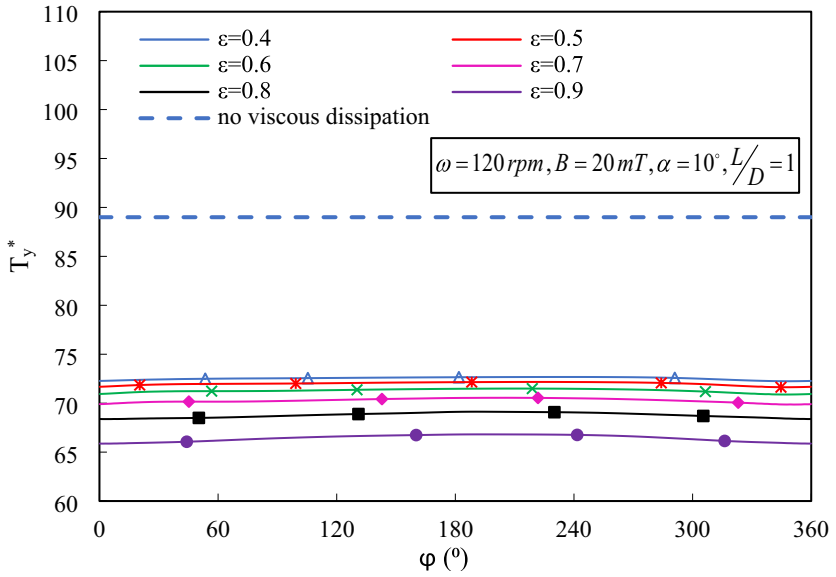

Fig. 23. Dimensionless yield stress versus angle of maximum clearance (ϕ) for various eccentricities and B = 20 mT. Solid lines represent outcomes when considering viscous dissipation, while dashed lines pertain to results when viscous dissipation is not taken into account.

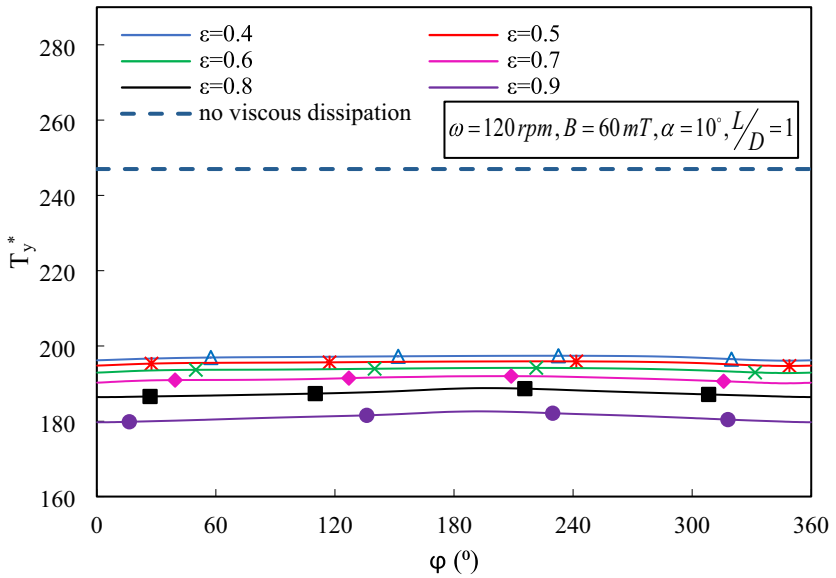

Fig. 24. Dimensionless yield stress versus angle of maximum clearance (ϕ) for various eccentricities and B = 60 mT. Solid lines represent outcomes when considering viscous dissipation, while dashed lines pertain to results when viscous dissipation is not taken into account.

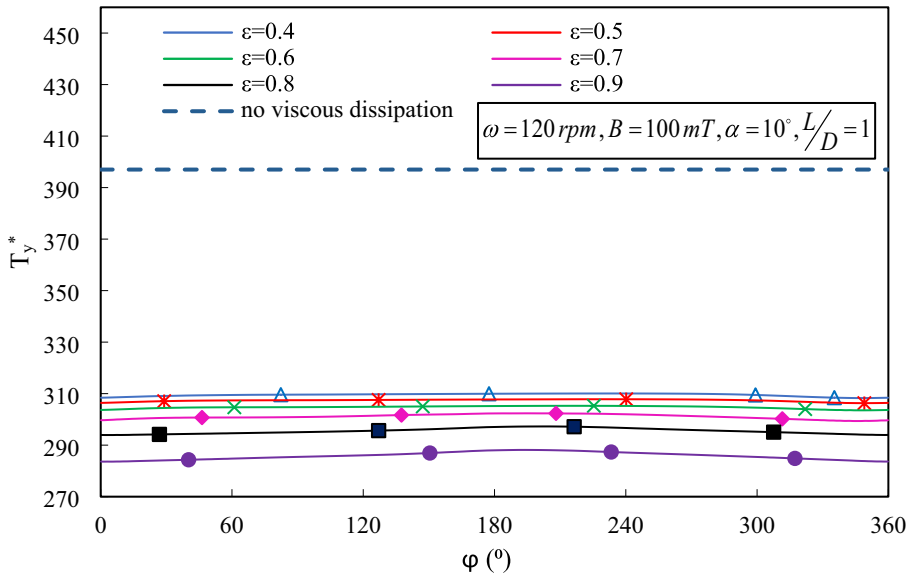

Fig. 25. Dimensionless yield stress versus angle of maximum clearance (ϕ) for various eccentricities and B = 100 mT. Solid lines represent outcomes when considering viscous dissipation, while dashed lines pertain to results when viscous dissipation is not considered.

material with no overall deformation. When analyzing the force equilibrium in this scenario, it becomes evident that two pressure gradients, namely circumferential and axial (∂p/∂θ and ∂p/∂z), play a crucial role in influencing the creation of plug regions.

In the absence of any circumferential pressure gradient, plug formation does not occur. However, the presence of these pressure gradients alters the shear stress pressure gradient along the radial direction, leading to the emergence of plug regions. A static plug region forms when there is a sufficiently high circumferential pressure gradient (greater than zero). As the circumferential pressure gradient intensifies, the shear stress eventually exceeds the yield stress. In such instances, the static plug region disengages from the bearing and transforms into a moving plug. Examination of fluid flow around this area reveals reverse flow during this transformation. The size of the plug diminishes with an increase in ∂p/∂θ; if this gradient is negative, the plug regions remain attached to the journal.

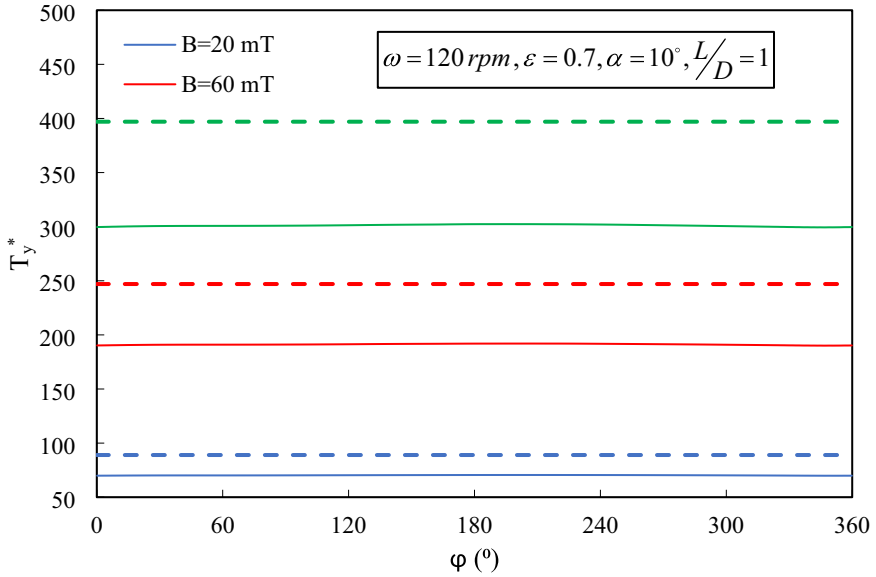

Fig. 26. Dimensionless yield stress versus angle of maximum clearance (ϕ) for various Magnetic field strengths. Solid lines represent outcomes when considering viscous dissipation, while dashed lines pertain to results when viscous dissipation is not considered.

Furthermore, the thickness and surface area occupied by the plug region are two critical parameters for predicting plug formation regions. The geometric characteristics of the bearing greatly influence these parameters. The presence of a plug region can significantly impact the bearing's performance, making it essential to alert the designer to take measures to prevent this occurrence.

The thickness (t) and surface area (s) occupied by the plug region are defined as:

$$s = \frac{A_b + A_f}{2\pi R_b L}, \tag{35}$$

$$t = \max\left(\frac{t(\theta)}{h(\theta)}\right), \tag{36}$$

where A_b and A_f are the area of the core adhered to bearing and the area of the floating core and $t(\theta)$ and $h(\theta)$ are core thickness and film thickness, respectively.

Amidst all the critical considerations related to plug formation, temperature is a pivotal factor that significantly affects the dimensions and thickness of occupied plug regions. An increase in temperature can result in a reduction in the viscosity and yield stress of MR fluids. Consequently, in the presence of viscous dissipation that leads to temperature elevation, MR fluids may exhibit a more facile flow behavior, potentially making detecting these plug regions more challenging.

In this context, the type of plug area, along with its influential parameters like aspect ratio, eccentricity, magnetic field, and viscous dissipation, is carefully considered.

Figures 27 and 28 depict how λ, ε, the magnetic field, and viscous dissipation exert their influence. A higher λ value leads to an expanded volume occupied by the plug region, possibly due to a more uniform pressure distribution along the Z-axis. Increasing the magnetic field results in higher yield stress, reducing the number of regions experiencing yield and increasing the plug region's area. The figures suggest that plug regions manifest at specific ε values, primarily under the influence of significant circumferential pressure gradients. As the circumferential pressure gradient increases, the plug regions shift from one side of the bearing to the other. Under static conditions, raising the ε value may cause the plug to divide into two or more segments, giving rise to moving plugs in between. In the figures depicting plugs, black represents static regions, while grey areas indicate moving plugs.

As evident from Figs. 27, 28, it becomes clear that viscous dissipation plays a crucial role in influencing the formation of plug regions. This influence arises from the temperature increase, which leads to a decrease in both viscosity and yield stress. For cases where $\lambda < 1$, plug formation is not detected, considering the impact of viscous dissipation. In contrast, for cases where $\lambda > 1$, the detected plugs tend to occur at lower eccentricities. This occurrence can be attributed to the elevated temperature resulting from increased eccentricity, reducing yield stress. Furthermore, these plugs exhibit reduced thickness and area. Notably, plug formation is more effective near the static wall, primarily due to the lower temperature in that region, resulting in the prevalence of nearly stationary plug regions. In certain instances, the area and thickness of plug regions may exhibit a reduction of approximately 50%.

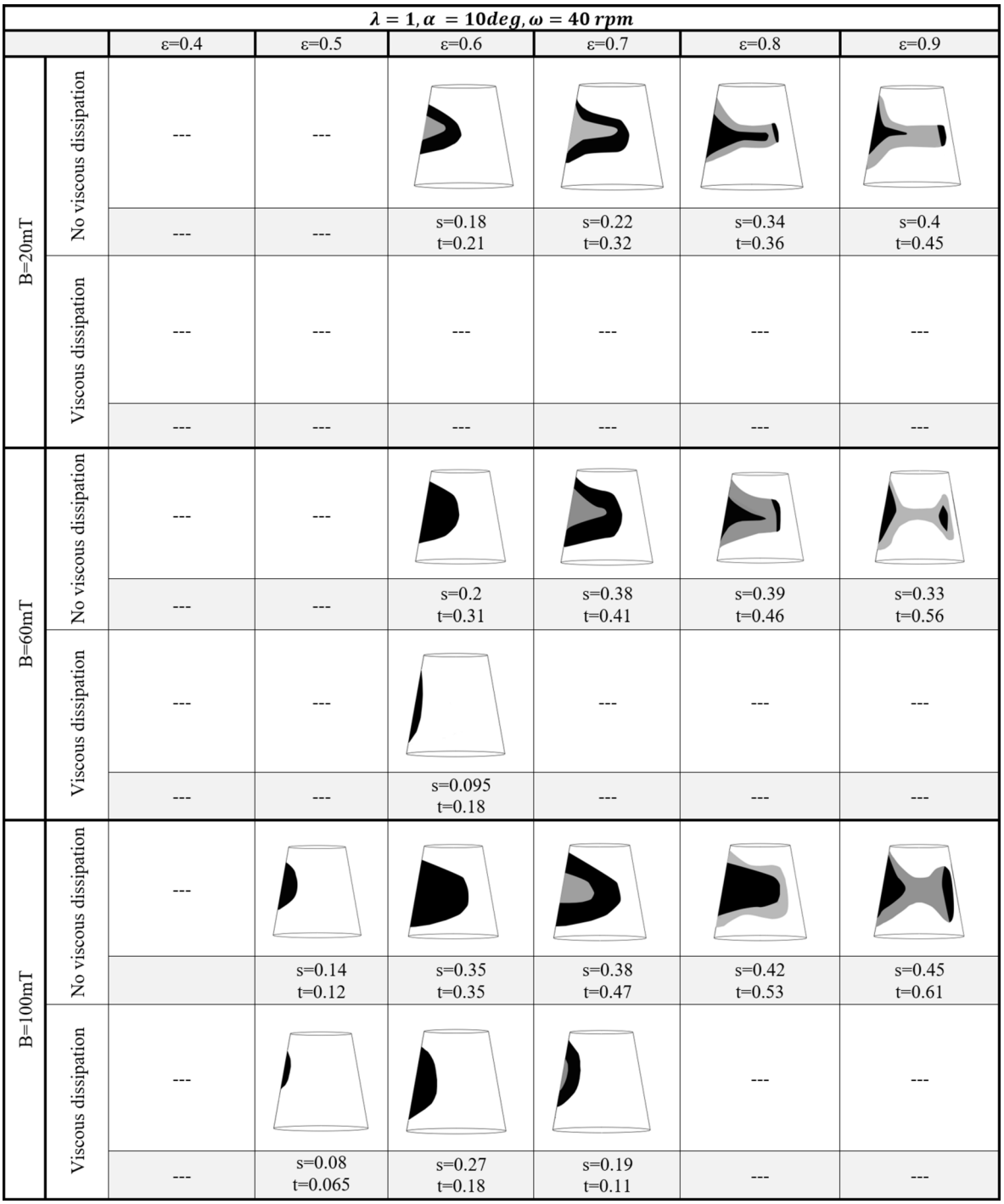

Fig. 27. Formation of static and moving plugs for λ = 1, α = 10, and ω = 40 rpm (areas shaded in black and grey denote static and moving plug regions, respectively).

Performance characteristics

Load-carrying capacity

As the temperature rises due to viscous dissipation, the viscosity of the MR fluid typically decreases. The combination of radial and axial load capacities determines the total load capacity of an MR bearing. Any changes in the viscosity of the MR fluid due to viscous dissipation can influence both radial and axial load capacities and, consequently, the total load-carrying capacity. Engineers may need to optimize the MR bearings design to account for viscous dissipation's impact on load capacity. This optimization may include selecting suitable MR fluids with temperature-dependent properties and designing bearing elements to withstand thermal effects.

Figure 29 shows the effects of eccentricity and aspect ratio on radial and axial load capacities. A higher aspect ratio in a conical bearing can typically lead to an increase in radial and axial load capacity. A more extended bearing with a higher aspect ratio provides more contact surface area between the journal and the fluid, which

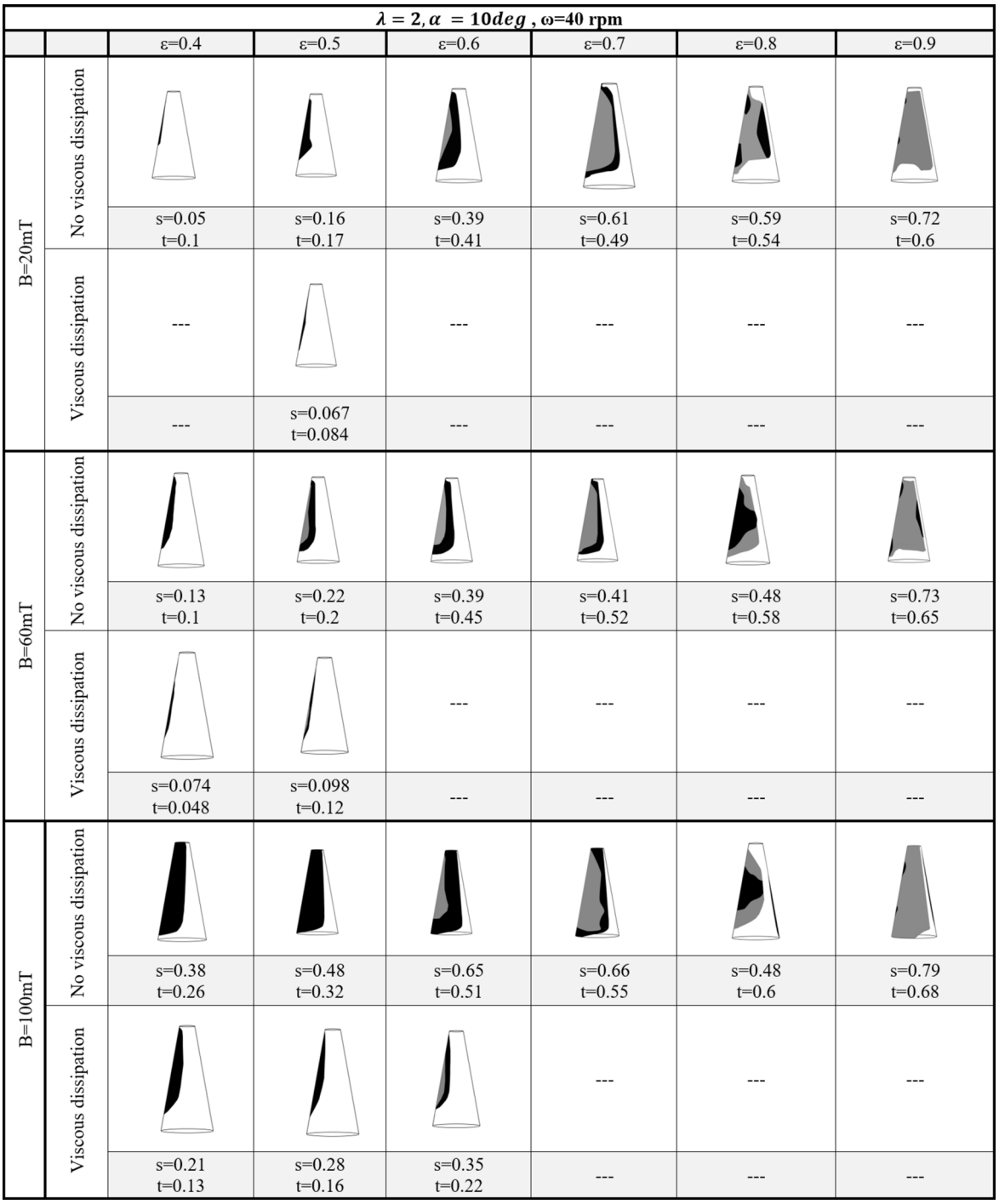

Fig. 28. Formation of static and moving plugs for λ = 2, α = 10, and ω = 40 rpm (areas shaded in black and grey denote static and moving plug regions, respectively).

enhances its ability to support radial and axial loads. Conversely, a lower aspect ratio may reduce the radial and load capacity, as it provides less surface area for load distribution, making it less effective at supporting radial and axial loads. For instance, the radial and axial load capacity for $\varepsilon = 0.9$ and λ = 2 is 93% greater than that for λ = 1/4. Also, the radial and axial load rises with the growth of eccentricity. Greater eccentricities result in higher load capacities. The radial and axial load capacity for $\lambda = 2$ and ε = 0.9 is 72% greater than that for ε = 0.4.

Figures 30, 31 and 32 depict the influence of cone angle on the radial, axial, and overall load capacities of MR conical bearings. In hydrodynamic conical bearings, an increase in the bearing cone angle leads to a decrease in load capacity due to the expansion of fluid film thickness and reduction in pressure magnitude. Consequently, there is a notable decline in radial load capacity (WR). Despite the enhancement in the axial component of load capacity (WA) with increased cone angle, it fails to compensate for the decrease in WR, resulting in the radial load component remaining dominant and causing a reduction in total load capacity with increasing cone angle.

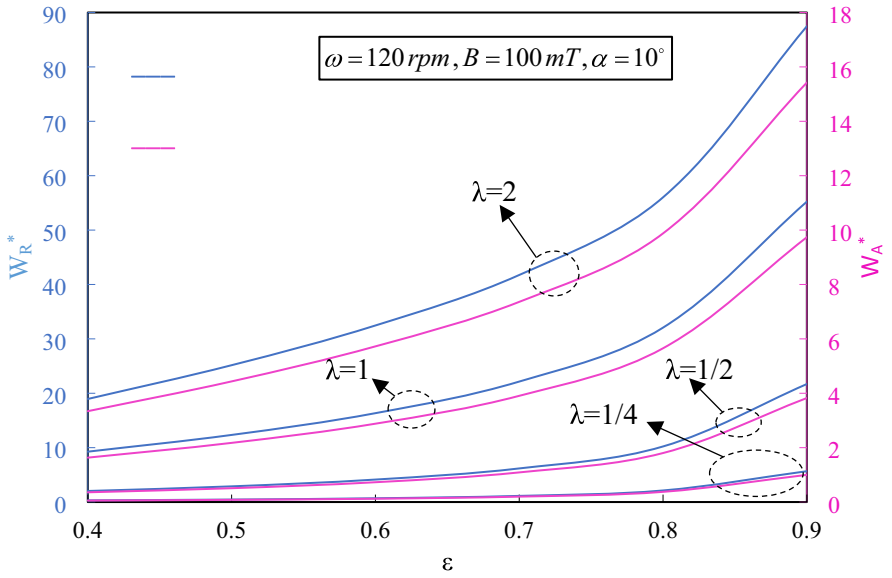

Fig. 29. Dimensionless radial and axial load capacities versus eccentricity for various aspect ratios.

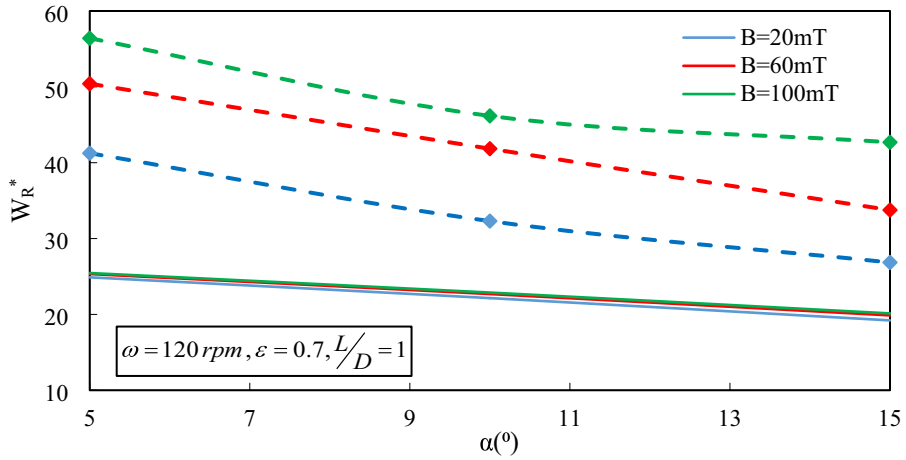

Fig. 30. Dimensionless radial load capacity versus cone angle for various magnetic fields. Solid lines represent outcomes when considering viscous dissipation, while dashed lines pertain to results when viscous dissipation is not considered.

The application of a magnetic field to MR conical bearings can increase radial load capacity. The magnetic field strengthens the MR effect, thereby improving the bearing's ability to withstand radial loads. It also enables real-time adjustment of radial load capacity, particularly beneficial for accommodating varying loads or operational conditions. Moreover, the magnetic field can influence the axial load capacity as well.In some cases, it may enhance the bearing's ability to carry axial loads. The dynamic control of axial load capacity through applying a magnetic field is valuable in applications that require adaptability to changing axial load conditions (Fig. 31). Viscous dissipation can affect the load capacity of an MR conical bearing by altering temperature and viscosity, impacting its ability to support radial and axial loads. As evident in Fig. 32, viscous dissipation can reduce the load capacity of the MR bearing by up to 55%.

Friction force

Figures 33 and 34 depict how eccentricity, magnetic field intensity, and aspect ratio affect frictional force. The frictional forces exerted on the journal's surface exceed those on the bearing's surface. With higher magnetic field strength, friction force increases due to the magnetic field's impact on elevating viscosity and shear rate, requiring a greater load to overcome heightened friction. Additionally, friction force amplifies with increasing eccentricity, particularly more pronounced at higher eccentricities.

Temperature exerts a direct influence on the viscosity of MR fluids. In general, as temperature rises, the viscosity of MR fluids declines. This reduction in viscosity can impact the MR fluid's capacity to provide the intended

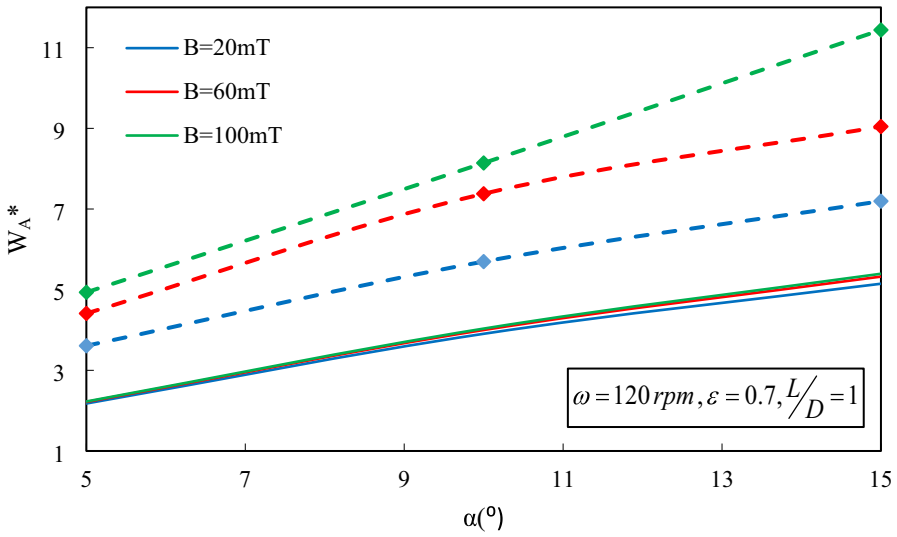

Fig. 31. Dimensionless axial load capacity versus cone angle for various magnetic fields. Solid lines represent outcomes when considering viscous dissipation, while dashed lines pertain to results when viscous dissipation is not considered.

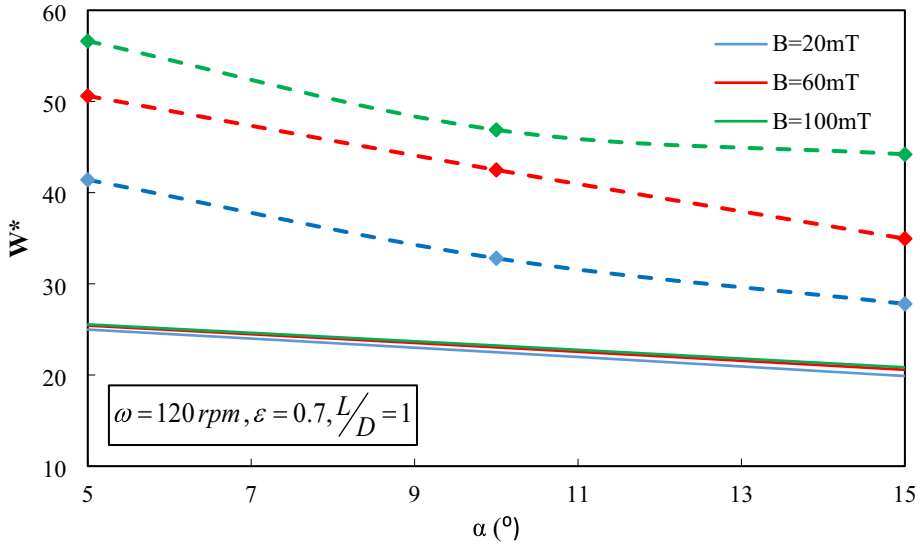

Fig. 32. Dimensionless total load capacity versus cone angle for various magnetic fields. Solid lines represent outcomes when considering viscous dissipation, while dashed lines pertain to results when viscous dissipation is not considered.

damping and load-bearing characteristics within the bearing, resulting in reduced frictional forces. Concurrently, temperature variations can induce changes in the rheological properties of the MR fluid, including yield stress and dynamic viscosity. These alterations affect the MR fluid's responsiveness to the applied magnetic field and, consequently, affect friction forces. In specific scenarios, temperature increases can offer beneficial lubricating effects. The resulting heat reduces the MR fluid's viscosity, causing it to behave more akin to a lubricant, reducing friction. The temperature rise can reduce the friction force by up to 75%.

Friction coefficient

Table 5 illustrates the variations in the normalized friction coefficient concerning the aspect ratio, eccentricity, and magnetic field flux density for both the bearing and journal. The discrepancy in friction coefficients between the bearing and journal primarily stems from the nonlinear virtual velocity distribution. Conversely, friction coefficient values notably decrease with increasing aspect ratio and eccentricity. However, an increase in magnetic field flux density results in higher friction coefficient values due to the heightened yield stress. Typically, as the temperature rises, the viscosity of MR fluid decreases, impacting the friction force coefficient. Lower viscosity often diminishes frictional forces, consequently leading to a lower friction force coefficient.

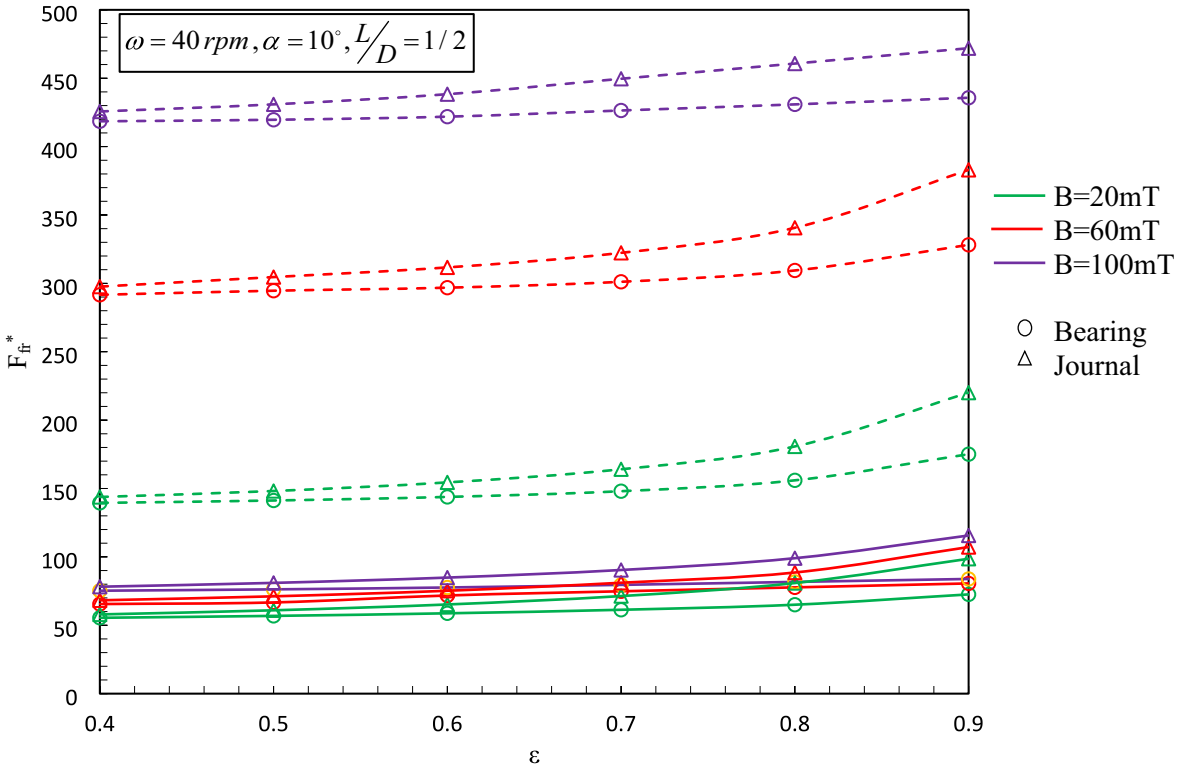

Fig. 33. Dimensionless friction force versus cone angle for various eccentricities, magnetic field, and λ = 1/2. Solid lines represent outcomes when considering viscous dissipation, while dashed lines pertain to results when viscous dissipation is not considered.

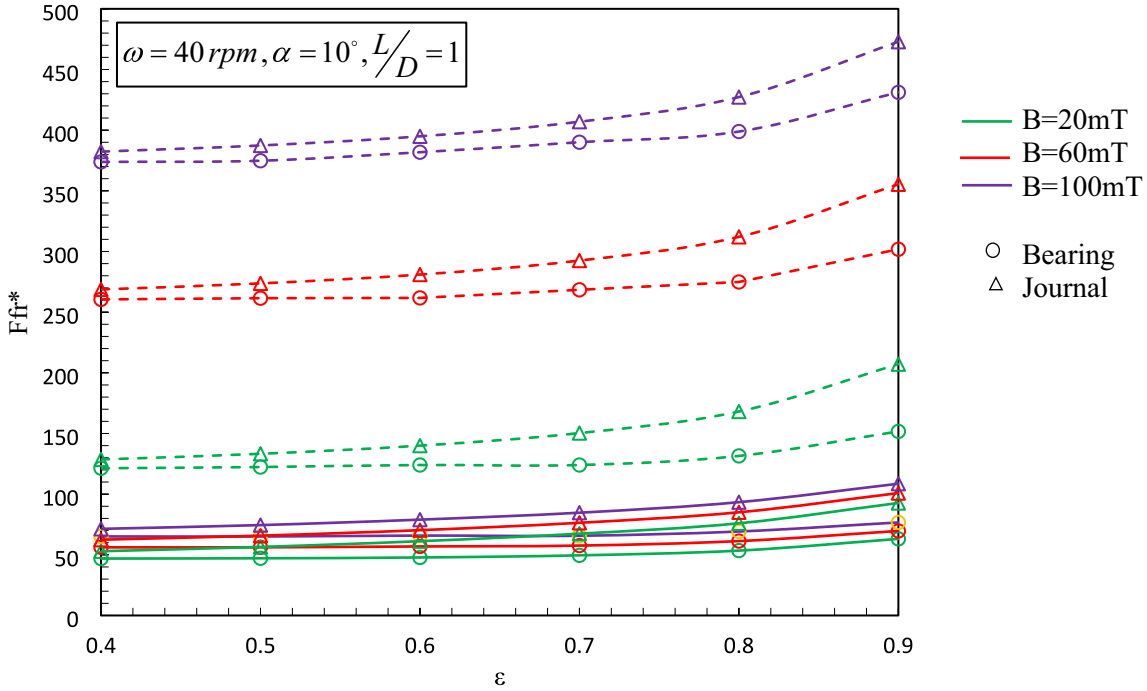

Fig. 34. Dimensionless friction force versus cone angle for various eccentricities, magnetic field, and λ = 1. Solid lines represent outcomes when considering viscous dissipation, while dashed lines pertain to results when viscous dissipation is not considered.

			L/D = 1/2		L/D = 1		L/D = 2	
			f_b	f_j	f_b	f_j	f_b	f_j
B = 20mT	No viscous dissipation	ε = 0.4	18.51	19.11	10.30	10.92	8.47	9.17
		ε = 0.5	13.72	14.41	7.62	8.31	6.51	7.27
		ε = 0.6	10.19	10.95	5.55	6.27	4.95	5.94
		ε = 0.7	7.31	8.11	3.78	4.59	2.88	3.98
		ε = 0.8	4.78	5.54	2.49	3.19	1.92	2.48
		ε = 0.9	2.40	3.02	1.44	1.97	1.25	1.71
	Viscous dissipation	ε = 0.4	13.42	14.01	4.99	5.64	3.34	3.38
		ε = 0.5	9.70	10.39	3.76	4.51	2.56	2.72
		ε = 0.6	6.99	7.76	2.88	3.69	2.09	2.34
		ε = 0.7	4.88	5.68	2.20	3.00	1.75	2.09
		ε = 0.8	3.13	3.90	1.64	2.33	1.43	1.83
		ε = 0.9	1.65	2.24	1.13	1.65	1.08	1.48
B = 40mT	No viscous dissipation	ε = 0.4	25.59	31.77	18.49	19.10	15.54	16.25
		ε = 0.5	19.21	19.86	13.47	14.11	11.25	11.85
		ε = 0.6	14.35	15.08	9.43	10.14	8.52	9.34
		ε = 0.7	10.31	11.05	6.32	6.89	5.51	6.02
		ε = 0.8	6.75	7.43	3.81	4.33	3.15	3.71
		ε = 0.9	3.39	3.95	2.06	2.43	1.86	1.96
	Viscous dissipation	ε = 0.4	7.28	14.93	5.80	6.46	4.41	4.44
		ε = 0.5	10.46	11.17	4.38	5.13	3.15	3.37
		ε = 0.6	8.03	8.42	3.36	4.16	2.39	2.66
		ε = 0.7	5.73	6.20	2.50	3.32	1.90	2.21
		ε = 0.8	3.69	4.21	1.83	2.53	1.52	1.89
		ε = 0.9	1.84	2.45	1.20	1.74	1.12	1.50
B = 60mT	No viscous dissipation	ε = 0.4	31.42	31.99	24.93	25.52	22.18	22.94
		ε = 0.5	23.44	24.09	18.05	18.68	16.52	17.56
		ε = 0.6	17.40	18.09	12.72	13.17	11.05	12.35
		ε = 0.7	12.38	13.07	8.32	8.69	7.12	7.92
		ε = 0.8	10.01	10.68	4.82	5.17	3.42	4.42
		ε = 0.9	8.27	8.96	2.51	2.75	1.86	1.95
	Viscous dissipation	ε = 0.4	15.30	15.91	6.74	7.39	5.61	5.63
		ε = 0.5	11.26	11.97	5.10	5.84	4	4.23
		ε = 0.6	8.29	9.07	3.88	4.66	2.77	3.13
		ε = 0.7	5.93	6.74	2.83	3.65	2.11	2.42
		ε = 0.8	3.81	4.62	2.02	2.73	1.63	1.97
		ε = 0.9	1.93	2.66	1.29	1.83	1.17	1.53

Table 5. Normalized friction coefficient on the journal and bearing for different aspect ratios, eccentricities, and magnetic field considering viscous dissipation effects.

In order to address the influence of temperature increases resulting from viscous dissipation on the friction force coefficient in a conical MR bearing, it is essential to consider elements like temperature regulation systems, material choices, and design enhancements. These strategies keep the bearing operating within a favorable temperature range, thereby minimizing potential fluctuations in the friction force coefficient and guaranteeing the dependable performance of the bearing.

Conclusions

This research tackled the lubrication issue in conical bearings using MR fluids while considering conjugate heat transfer (CHT). Given the intricate nature of the problem, the Finite Element Method (FEM) was employed to solve the Cauchy equations of motion, energy equation, and Maxwell equation. The study delved into the effects of various parameters, leading to the acquisition of significant findings; these findings offer valuable insights into the behavior of conical hydrodynamic bearings with MR lubricants and can guide future research to optimize their performance.

- The influence of temperature on the lubrication of conical bearings using MR fluid can be substantial and warrants meticulous attention when designing and operating these systems.

- Temperature variations can affect the rheological behavior of MR fluid, including viscosity, yield stress, plug regions, friction forces, and load capacity.
- With rising the temperature, the MR fluid's viscosity usually declines, resulting in reduced viscosity and a decrease in yield stress.
- Viscous dissipation is a significant factor in MR fluids. It may increase due to magnetic fields and angular velocities, leading to higher viscosity, while it can also raise the temperature, resulting in reduced viscosity. Ultimately, it is crucial to manage and control viscous dissipation.
- Radial and circumferential pressure gradients are pivotal in delineating static and moving plug regions, thus alterations in these gradients can reshape the area of plug formation.
- A heightened L/D ratio leads to a larger occupied region by plugs within the bearing, influenced by various parameters that gain significance at specific ε values. Increased ε values may fragment static plug regions into multiple pieces, giving rise to moving plugs in between. Moreover, elevating circumferential pressure gradients causes static plug regions to shift along the circumferential direction. These findings provide valuable insights into the behavior of conical hydrodynamic bearings with MR lubricants, offering guidance for future optimization efforts.
- Augmented viscous dissipation can bolster heat transfer, resulting in decreased viscosity and yield stress of MR fluid, thereby inhibiting plug formation in many cases and inducing yielding behavior across the entire fluid domain.
- Compared to conventional lubricants, MR lubricants can elevate the load-carrying capacity of conical hydrodynamic bearings, with radial forces exerting a predominant influence over axial forces. Nevertheless, meticulous regulation of temperatures within specified bounds is imperative.
- Heightening magnetic field strength in MR fluids increases virtual viscosity, leading to amplified friction forces on the bearing and journal walls. These forces may have varying effects contingent on temperature fluctuations; reducing virtual viscosity through temperature reduction can be advantageous, while high shear rates may trigger temperature elevation and adverse effects.
- Integration of conical bearings and MR fluids for lubrication control presents an array of potential industrial applications for these bearings.

Data availability

The datasets generated and/or analyzed during the current study are not publicly available due to the local data safety agreement but are available from the corresponding author on reasonable request.

Received: 26 April 2024; Accepted: 30 August 2024
Published online: 04 September 2024

References

1. Knight, J. & Niewiarowski, A. Effects of two film rupture models on the thermal analysis of a journal bearing. *J. Tribol.* https://doi.org/10.1115/1.2920240 (1990).
2. Kim, J., Palazzolo, A. B. & Gadangi, R. K. TEHD analysis for tilting-pad journal bearings using upwind finite element method. *Tribol. Trans.* **37**, 771–783 (1994).
3. Suh, J. & Palazzolo, A. Three-dimensional dynamic model of TEHD tilting-pad journal bearing—Part I: Theoretical modeling. *J. Tribol.* **137**, 041703 (2015).
4. Suh, J. & Palazzolo, A. Three-dimensional dynamic model of TEHD tilting-pad journal bearing—Part II: Parametric studies. *J. Tribol.* **137**, 041704 (2015).
5. Mitsui, J., Hori, Y. & Tanaka, M. Thermohydrodynamic analysis of cooling effect of supply oil in circular journal bearing. *J. Lubr. Technol.* https://doi.org/10.1115/1.3254629 (1983).
6. Nassab, S. G. & Moayeri, M. Three-dimensional thermohydrodynamic analysis of axially grooved journal bearings. *Proc. Inst. Mech. Eng. J J. Eng. Tribol.* **216**, 35–47 (2002).
7. Fatu, A., Hajjam, M. & Bonneau, D. A new model of thermoelastohydrodynamic lubrication in dynamically loaded journal bearings (2006).
8. Brito, F., Miranda, A., Bouyer, J. & Fillon, M. Experimental investigation of the influence of supply temperature and supply pressure on the performance of a two-axial groove hydrodynamic journal bearing (2007).
9. Liu, D., Zhang, W. & Zheng, T. A simplified one-dimensional thermal model for journal bearings. *J. Tribol.* https://doi.org/10.1115/1.2805427 (2008).
10. Chauhan, A., Sehgal, R. & Sharma, R. K. Investigations on the thermal effects in non-circular journal bearings. *Tribol. Int.* **44**, 1765–1773 (2011).
11. Jeng, M.-C. & Yang, Y.-K. Comparison of thermal effects on the conical-cylindrical bearing with 2-D and 3-D energy equations. *Tribol. Trans.* **45**, 67–75 (2002).
12. Yang, Y.-K. & Jeng, M.-C. Analysis of viscosity interaction and heat transfer on the dual conical-cylindrical bearing©. *Tribol. Trans.* **47**, 77–85 (2004).
13. Tarawneh, C. M., Cole, K. D., Wilson, B. M. & Alnaimat, F. Experiments and models for the thermal response of railroad tapered-roller bearings. *Int. J. Heat Mass Transf.* **51**, 5794–5803 (2008).
14. Gao, P. *et al.* Theoretical and experimental investigation on thermal characteristics of railway double-row tapered roller bearing. *Energies* **15**, 4217 (2022).
15. Hirano, T., Guo, Z. & Kirk, R. G. Application of computational fluid dynamics analysis for rotating machinery—Part II: Labyrinth seal analysis. *J. Eng. Gas Turbines Power* **127**, 820–826 (2005).
16. Uhkoetter, S. *et al. Turbo Expo: Power for Land, Sea, and Air* 749–758 (American Society of Mechanical Engineers, 2012).
17. Liu, H., Xu, H., Ellison, P. J. & Jin, Z. Application of computational fluid dynamics and fluid–structure interaction method to the lubrication study of a rotor–bearing system. *Tribol. Lett.* **38**, 325–336 (2010).
18. Deligant, M., Podevin, P. & Descombes, G. CFD model for turbocharger journal bearing performances. *Appl. Therm. Eng.* **31**, 811–819 (2011).

19. Papadopoulos, C., Kaiktsis, L. & Fillon, M. Computational fluid dynamics thermohydrodynamic analysis of three-dimensional sector-pad thrust bearings with rectangular dimples. *J. Tribol.* **136**, 011702 (2014).
20. Gengyuan, G., Zhongwei, Y., Dan, J. & Xiuli, Z. CFD analysis of load-carrying capacity of hydrodynamic lubrication on a water-lubricated journal bearing. *Ind. Lubr. Tribol.* **67**, 30–37 (2015).
21. Yang, J. & Palazzolo, A. Deep convolutional autoencoder augmented CFD thermal analysis of bearings with inter pad groove mixing. *Int. J. Heat Mass Transf.* **188**, 122639 (2022).
22. Guo, Z., Hirano, T. & Kirk, R. G. Application of CFD analysis for rotating machinery—Part I: Hydrodynamic, hydrostatic bearings and squeeze film damper. *J. Eng. Gas Turbines Power* **127**, 445–451 (2005).
23. Song, Y. & Gu, C.-W. Development and validation of a three-dimensional computational fluid dynamics analysis for journal bearings considering cavitation and conjugate heat transfer. *J. Eng. Gas Turbines Power* **137**, 122502 (2015).
24. Liu, W. *et al.* Lubrication characteristics and thermal deformation of hydrostatic thrust bearing based on conjugate heat transfer. *Ind. Lubr. Tribol.* https://doi.org/10.1108/ILT-10-2022-0313 (2023).
25. Wang, X. *et al.* Dynamic characteristics of magnetorheological fluid lubricated journal bearing and its application to rotor vibration control. *J. Vibroeng.* **17**, 1912–1928 (2015).
26. Bompos, D. A. & Nikolakopoulos, P. G. Rotordynamic analysis of a shaft using magnetorheological and nanomagnetorheological fluid journal bearings. *Tribol. Trans.* **59**, 108–118 (2016).
27. Wang, X., Li, H., Lu, W. & Meng, G. Stiffness and damping properties of (semi) floating ring bearing using magnetorheological fluids as lubricant. *J. Tribol.* https://doi.org/10.1115/1.4035773 (2017).
28. Wang, X., Li, H. & Meng, G. Rotordynamic coefficients of a controllable magnetorheological fluid lubricated floating ring bearing. *Tribol. Int.* **114**, 1–14 (2017).
29. Urreta, H., Aguirre, G., Kuzhir, P. & Lopez de Lacalle, L. N. Actively lubricated hybrid journal bearings based on magnetic fluids for high-precision spindles of machine tools. *J. Intell. Mater. Syst. Struct.* **30**, 2257–2271 (2019).
30. Sahu, K., Sharma, S. C. & Ram, N. Misalignment and surface irregularities effect in MR fluid journal bearing. *Int. J. Mech. Sci.* **221**, 107196 (2022).
31. Li, W., Chen, G., Yeo, S. & Du, H. Temperature dependence of MR fluids. *Int. J. Mod. Phys. B* **16**, 2725–2731 (2002).
32. Wilson, N. L., Wereley, N. M., Hu, W. & Hiemenz, G. J. Analysis of a magnetorheological damper incorporating temperature dependence. *Int. J. Veh. Des.* **63**, 137–158 (2013).
33. Bompos, D. A. & Nikolakopoulos, P. G. In *Proc. of the 9th IFToMM International Conference on Rotor Dynamics*, 1135–1144 (Springer).
34. Mitrouchev, P. *et al.* Analytical research of damping efficiency and heat generation of magnetorheological damper. *Smart Mater. Struct.* **26**, 065026 (2017).
35. Wang, N., Liu, X., Królczyk, G., Li, Z. & Li, W. Effect of temperature on the transmission characteristics of high-torque magnetorheological brakes. *Smart Mater. Struct.* **28**, 057002 (2019).
36. Sahu, K. & Sharma, S. C. Magneto-rheological fluid slot-entry journal bearing considering thermal effects. *J. Intell. Mater. Syst. Struct.* **30**, 2831–2852 (2019).
37. Zschunke, F., Rivas, R. & Brunn, P. Temperature behavior of magnetorheological fluids. *Appl. Rheol.* **15**, 116–121 (2005).
38. Sahin, H., Wang, X. & Gordaninejad, F. Temperature dependence of magneto-rheological materials. *J. Intell. Mater. Syst. Struct.* **20**, 2215–2222 (2009).
39. Bahiuddin, I., Mazlan, S., Shapiai, I., Imaduddin, F. & Choi, S.-B. Constitutive models of magnetorheological fluids having temperature-dependent prediction parameter. *Smart Mater. Struct.* **27**, 095001 (2018).
40. Li, H., Jönkkäri, I., Sarlin, E. & Chen, F. Temperature effects and temperature-dependent constitutive model of magnetorheological fluids. *Rheol. Acta* **60**, 719–728 (2021).
41. Vaziri, S. A., Norouzi, M., Akbarzadeh, P., Kim, M. & Kim, K. C. Numerical analysis of conical hydrodynamic bearing lubricated with magnetorheological fluid. *J. Braz. Soc. Mech. Sci. Eng.* **46**, 1–29 (2024).
42. Laukiavich, C., Braun, M. J. & Chandy, A. J. A comparison between the performance of ferro-and magnetorheological fluids in a hydrodynamic bearing. *Proc. Inst. Mech. Eng. J J. Eng. Tribol.* **228**, 649–666 (2014).
43. Gertzos, K., Nikolakopoulos, P. & Papadopoulos, C. CFD analysis of journal bearing hydrodynamic lubrication by Bingham lubricant. *Tribol. Int.* **41**, 1190–1204 (2008).
44. Urreta, H. *et al.* Hydrodynamic bearing lubricated with magnetic fluids. *J. Intell. Mater. Syst. Struct.* **21**, 1491–1499 (2010).
45. Sharma, S. C. & Kumar, A. On the behaviour of roughened conical hybrid journal bearing system operating with MR lubricant. *Tribol. Int.* **156**, 106824 (2021).
46. Sahu, K., Sharma, S. C. & Tomar, A. K. Analysis of MR fluid lubricated slot entry hybrid conical journal bearing with texturing arrangement. *Tribol. Int.* **188**, 108788 (2023).
47. Sharma, S. C. & Tomar, A. K. Study on MR fluid hybrid hole-entry spherical journal bearing with micro-grooves. *Int. J. Mech. Sci.* **202**, 106504 (2021).
48. Arteaga, O. *et al. IOP Conference Series: Materials Science and Engineering* Vol. 012006 (IOP Publishing, 2019).
49. Wada, S., Hayashi, H. & Haga, K. Behavior of a Bingham solid in hydrodynamic lubrication: Part 2, application to step bearing. *Bull. JSME* **16**, 432–440 (1973).
50. Stout, K. & Rowe, W. Externally pressurized bearings—Design for manufacture part 1—Journal bearing selection. *Tribology* **7**, 98–106 (1974).
51. Li, Q., Zhang, S., Wang, Y., Xu, W.-W. & Wang, Z. Investigations of the three-dimensional temperature field of journal bearings considering conjugate heat transfer and cavitation. *Ind. Lubr. Tribol.* **71**, 109–118 (2019).
52. Ferron, J., Frene, J. & Boncompain, R. A study of the thermohydrodynamic performance of a plain journal bearing comparison between theory and experiments. *J. Lubr. Technol.* **105**, 422–428 (1983).

Acknowledgements

This work was supported by Brain Pool Program through the National Research Foundation of Korea (NRF) funded by Ministry of Science and ICT (NRF-2022H1D3A2A01091637). This work was also supported by the National Research Foundation of Korea (NRF) grant, which is funded by the Korean government (MSIT) (No. 2020R1A5A8018822, No. 2021R1C1C2009287). The authors also appreciated the financial support from the Shahrood University of Technology.

Author contributions

1. Seyyed Amirreza Vaziri: Implementation of analytical solution, presenting the results and physical dissuasion, and writing the paper. 2. Mahmood Norouzi: Supervisor, presenting the idea of the problem, presenting the method of the solution, conducting the research, scientific discussion, and editing. 3. Pooria Akbarzadeh: Advisor, conducting the research, scientific discussion, and editing. 4. Kyung Chun Kim: Scientific discussion

and interpretation of the results, modification, and English editing. 5. Mirae Kim: Scientific discussion and interpretation of the results, modification, and English editing.

Competing interests
The authors declare no competing interests.

Additional information
Correspondence and requests for materials should be addressed to M.K.

Reprints and permissions information is available at www.nature.com/reprints.

Publisher's note Springer Nature remains neutral with regard to jurisdictional claims in published maps and institutional affiliations.